Shear localization as a key control on mass-transport complexes seal integrity: insights from geophysical datasets

Zhenghao Han[1], Nan Wu[1*], Jinfeng Ren[2,3], Zenggui Kuang[2,3]

[1]State Key Laboratory of Marine Geology, Tongji University, 1239 Siping Road, Shanghai, 200092, China

[2]National Engineering Research Center of Gas Hydrate Exploration and Development, Guangzhou Marine Geological Survey, Guangzhou, 511458, China

[3]Key Laboratory of Marine Mineral Resources, Ministry of Natural Resources, Guangzhou, 510075, China

*Nan Wu (nanwu@tongji.edu.cn)

Abstract

Mass-transport complexes (MTCs), existing in all sedimentary basins worldwide, can serve as effective seals for hydrocarbons and carbon dioxide storage due to shear-induced overcompaction. However, localized seal failure is occasionally observed in specific part of the MTCs, leading to hydrocarbon and carbon dioxide leakage and posing potential threats to seabed stability. Due to the scarcity of borehole data that penetrate MTCs, their petrophysical properties remain poorly constrained, and the factors controlling their seal integrity are still not well understood. This study integrates 3D seismic and well log data to investigate the petrophysical characteristics of three stacked MTCs in the Qiongdongnan Basin, northern South China Sea, aiming to identify the key factors that control their seal integrity. Seismic interpretation reveals that the seal integrity of MTCs tends to fail in areas where frontal ramps or remnant blocks are present, whereas the remaining parts remain intact and effectively seal the underlying free gas and gas hydrate. Petrophysical analyses show that MTCs with frontal ramps or remnant blocks exhibit significantly lower compaction (i.e., reduced density and resistivity, increased porosity and permeability), suggesting a strong link between seal failure and the presence of these structures. Numerical simulations indicate that during MTC emplacement, shear localization develops in the lowermost part, forming a narrow, highly deformed band along the base of MTCs. The presence of remnant blocks and ramps and associated topographic highs can interrupt shear localization, causing segmentation of the basal shear zone. This segmentation reduces shear strain and compaction above these topographic highs, thereby compromising the seal integrity of the

MTCs. Therefore, shear localization is the key factor controlling the seal integrity of MTCs. Topographic highs along the basal shear surface can disrupt this process, significantly affecting hydrocarbon distribution and the feasibility of carbon dioxide storage.

1 Introduction

Mass-transport complexes (MTCs) are intensely deformed sedimentary bodies generated by the downslope movement of unstable sediments under gravity (Talling et al., 2007; Bull et al., 2009; Dugan, 2012). MTCs can cover areas ranging from a few square kilometers to over ten thousand square kilometers, with volumes reaching up to several hundred cubic kilometers (Karstens et al., 2023; Sager et al., 2022; Walton et al., 2024). Borehole-based studies indicate that while most MTCs are mud-rich, some are sand-prone and contain large, sandstone blocks (Wu et al., 2021). Mud-rich MTCs typically exhibit elevated resistivity, P-wave velocity, and density, along with reduced porosity and water content compared to the surrounding strata (Dugan et al., 2012; Wu et al., 2021). Additionally, the lower intervals of mud-rich MTCs are characterized by the highest P-wave velocity and density along with the lowest porosity, representing the most compacted structure named basal shear zone (Wu et al., 2021). In contrast, the internal sand-rich blocks typically exhibit lower P-wave velocity and density, higher porosity and permeability compared to the surrounding matrix (i.e., debrites), suggesting they are undercompacted and may maintain high reservoir space (Wu et al., 2021). Therefore, MTCs and their associated basal shear zone are considered effective seals for hydrocarbons, while the sand-rich blocks are considered potential reservoirs for hydrocarbon accumulation.

Although MTCs are generally considered effective hydrocarbon seals due to their high compaction and low permeability, recent studies have shown that seal failure may occur in specific part of MTCs. For example, fluid escape features such as pockmarks, gas chimneys, and acoustic anomalies are observed within MTCs, indicating vertical fluid migration and local seal failure (Lastras et al., 2004; Noda et al., 2013; Pattier et al., 2013). The apparent contradiction between the compacted, low-permeability nature of MTCs and the observed indicators of fluid migration prompts an important question: when do MTCs serve as effective seals, and what conditions lead to their failure? To address the above questions, we focus on the Songnan Low Uplift region in the Qiongdongnan Basin, South China Sea, where vertically stacked MTCs are interbedded with gas hydrate-bearing layers and have been repeatedly breached by fluid migration (Yang et al., 2013; Kuang et al. 2023). We integrate 3D seismic reflection and well log data to characterize the morphological and petrophysical properties of the MTCs, evaluate their seal integrity based on petrophysical assessment, and ultimately identify the key factors that control their seal integrity.

Our results reveal that during MTC emplacement, the lowermost interval is subject to a strain-focusing mechanism known as shear localization. This process typically occurs along the basal interval beneath relatively flat topography and gives rise to a highly deformed band that corresponds to the basal shear zone previously identified by Wu et al. (2021), which plays a key role in controlling the mechanical and sealing behavior of MTCs. However, basal topographic highs, including frontal ramps and remnant blocks, may interrupt shear localization and result in reduced compaction above these structures. Thus, MTCs function as effective seals when shear localization proceeds normally during emplacement, promoting the formation of a continuous basal shear zone. However, this seal integrity can fail when topographic highs disrupt shear localization and interrupt the continuity of the basal shear zone. Understanding the conditions under which MTCs maintain or lose their seal integrity is critical for evaluating subsurface fluid migration pathways, hydrocarbon trap integrity, and gas hydrate system evolution in deep-water basins. These insights also aid in evaluating gas hydrate reservoirs and guiding site selection for future subsea carbon storage.

2 Geological Setting

QDNB is a Cenozoic rift basin characterized by thick Paleogene to Quaternary sediments (6000~12,000 m) situated atop a Mesozoic igneous basement in the northern South China Sea (Huang et al., 2016). Due to regional erosion caused by the uplift of the Tibetan Plateau and the associated

East Asia monsoon, substantial volumes of siliceous sediment are transported from the southwestern Yangtze Block through the Red River system with additional sources from eastern Indochina Block and Hainan (Figure 1a; Su et al., 2019).

Multiple phases of rifting and post-rift thermal subsidence have shaped the basin, forming a complex network of normal faults and fracture zones (Yang et al., 2022). These faults act as major conduits for vertical fluid migration, as evidenced by the widespread development of gas chimneys and fault-rooted seepage structures (Cartwright & Santamarina, 2015; Kuang et al., 2023; Serov et al., 2023). Focused fluid flow along these faults promotes gas hydrate formation and overpressure buildup within sediments, both of which contribute to reduced slope stability (Chapp et al., 2008; Hustoft et al., 2009; Mountjoy et al., 2014). The interplay between high sedimentation rates, active faulting, and intense fluid activity in the QDNB thus creates favorable conditions for submarine slope failure and the development of MTCs (Chang et al., 2021; Hunt et al., 2013).

The study area specifically focuses on the Songnan Low Uplift within the QDNB, which encompasses key zones targeted for gas hydrate exploration in the South China Sea (Figure 1b). Since 2013, the Guangzhou Marine Geological Survey has identified multiple conventional gas fields and gas hydrate reservoirs in the QDNB, underscoring the region's significance in natural hydrocarbon accumulation (Figure 1b). Seismic and well log data suggest that MTCs are widely developed in the Songnan Low Uplift and often occur in close spatial association with gas hydrate-bearing intervals (Kuang et al., 2023; Ren et al., 2024). This spatial configuration implies a possible sealing relationship, where MTCs may serve as low-permeability barriers that help trap upward-migrating free gas and maintain gas hydrate stability beneath them.

3 Data and Methods

3.1 Seismic data and well log data

We adopt 3D seismic data provided by Guangzhou Marine Geological Survey. The 3D seismic data were collected from the Songnan Low Uplift region in 2018, covering an area of approximately 360 km² with water depths ranging from 1,650 to 1,800 m (Figure 1b). The 3D seismic data are post-stack time-migrated and zero-phase processed with positive amplitudes represented by a red and yellow peak and negative amplitudes represented by a blue and grey trough (Figure 2). The 3D seismic surveys have a dominant frequency of 40 Hz and an average seismic velocity of 1,660 m/s near the seabed sediment, which gives an approximate vertical resolution of c. 10 m for the near seabed sediments.

The adopted well log data were acquired using Schlumberger tools from four wells (W1, W2, W3, W4), including density, resistivity, neutron, acoustic, nuclear magnetic measurements, and in-situ temperature measurements (Figure 1b). To establish the relationship between depth domain (true vertical depth; TVD) well log data and time domain (two-way traveltime; TWT) seismic data, seismic-well tie is performed respectively for each well. Seismic-well tie begins with creating a synthetic seismogram using sonic and density logs to simulate how seismic waves travel through subsurface geobodies at the well site (Lines & Newrick, 2004). This synthetic seismogram is then compared to the actual seismic data collected near the well. By aligning the synthetic seismogram with the actual seismic trace, we can ensure that seismic reflections accurately match the geological layers observed in the well, enhancing the reliability of subsurface interpretations (see **Appendix A** for details).

3.2 Seismic attributes analysis

Seismic attributes are quantitative measurements derived from seismic data to reveal subsurface structures and properties that may not be immediately apparent in raw datasets (Chopra & Marfurt, 2007). In this study, we use variance and spectral decomposition with RGB blending to enhance the interpretation of complex geological features such as MTCs and fluid escape pipes.

The variance attribute measures the variability or heterogeneity within seismic traces, making it ideal for highlighting discontinuities (Chopra & Marfurt, 2007). For MTCs, high variance often corresponds to chaotic zones caused by sediment mixing during transport (Chopra & Marfurt, 2007; Chen et al., 2022). For fluid escape pipes, these features create vertical disturbances in seismic data, which manifest as zones of high variance (Cartwright et al., 2007; Cartwright & Santamarina, 2015). By applying variance attribute, we identify the spatial extent, boundaries, internal architecture of MTCs and enhance the visibility of fluid escape pipes.

Spectral decomposition is a frequency based seismic attribute analysis technique that breaks down seismic data into its individual frequency components (Anomneze et al., 2025). RGB blending is a visualization technique that builds on spectral decomposition to create an intuitive representation of frequency content (Bataller et al., 2019). In this method, three narrow frequency bins are split from the decomposed seismic data and assigned to the red (R), green (G), and blue (B) color channels, respectively (Bataller et al., 2019). Areas with similar frequency characteristics then appear in similar colors, allowing us to quickly spot patterns, transitions, or heterogeneities, such as intra-MTCs structures or fluid escape pipes (Eckersley et al., 2018).

3.3 Permeability calculation

Permeability represents a direct quantitative indicator for evaluating seal integrity (Schowalter, 1979). However, in situ measurements of permeability in fine-grained MTCs are difficult and costly to perform. To yield accurate permeability estimation for MTCs, we calculate the permeability from nuclear magnetic resonance measurements through empirical Schlumberger-Doll Research equation developed by Kenyon et al. (1988):

$$k = A\phi^4 (T_{2LM})^2 \tag{1}$$

where φ $[m^3 \cdot m^{-3}]$ is the porosity, T_{2LM} $[ms]$ is the logarithmic mean of the T_2 distribution, and A $[m^2 \cdot m^{-2}]$ is the fitting coefficient.

The investigated MTCs here exhibit elevated clay content (Kuang et al., 2023). For the determination of fitting coefficient a, we implement the function of lithology developed by Daigle and Dugan (2009) specifically for silt- and clay-rich sediments:

$$A = -2.7 \times 10^{-1}\ GR + 2.4 \times 10^{-16} \tag{2}$$

where GR $[gAPI]$ is the gamma ray log value.

3.4 Numerical modelling

To approximate the shear deformation within MTCs flowing over topographically variable strata, we implement a two-dimensional numerical solver based on implicit pseudo-transient methods and finite difference discretization (Räss et al., 2022; Liu et al., 2024). We describe failing MTCs as an incompressible, nonlinear, viscous fluid (Iverson, 1997). Under these assumptions, the momentum equations at steady state can be simplified to:

$$\frac{\partial \tau_{ij}}{\partial x_j} - \frac{\partial p}{\partial x_i} + F_i - \rho\left(u_j \frac{\partial u_i}{\partial x_j}\right) = 0 \tag{3}$$

where τ_{ij} $[Pa]$ is the deviatoric stress tensor, p $[Pa]$ is the isotropic pressure, $F_i = \rho g(sin\ \alpha, cos\ \alpha)$ $[kg \cdot s^{-2} \cdot m^{-2}]$ is the gravitational body force at a tilted angle α, $u_j \frac{\partial u_i}{\partial x_j}$ $[m \cdot s^{-2}]$ is the convective acceleration term, and $i \in \{x, z\}$ indexes the two spatial components.

Herein, we describe failing sediments as fluid with Herschel-Bulkley rheology behavior. Failing sediments behave as a fluid (i.e., $\tau > \tau_0$), thus neglecting the state of rigid solid. The rheology model for simple shear is implemented using:

$$\tau_{ij} = \tau_0 + k_0 \dot{\varepsilon}_{ij}^n \tag{4}$$

where τ_0 is the yield shear stress $[Pa]$, k_0 is the consistency index $[Pa \cdot s^n]$, n is the flow index $[dimensionless]$. The key physical parameters of modelled fluid can be found in Table 1.

Failing sediments flow into the domain from the left boundary over undeforming strata and exits at the right boundary. The analytical inflow field is calculated by solving the momentum balance along the flow at steady state. The outlet boundary condition is following the approach of Kreiss (1968), Gustafsson et al. (1972), and Orlanski (1976).

To prescribe the interface between MTCs and undeformed strata, we implement the immersed-boundary method, a fictitious domain method that allows us to treat fluid and solid domains separately and efficiently (Peskin, 1972, 2002). This method facilitates the independent and computationally efficient handling of fluid and solid domains, making it well-suited for addressing the intricate geometries and dynamic interactions prevalent in MTCs (Peskin, 1972, 2002; Zhao et al., 2021).

The detailed explanations of numerical simulation considering pseudo-transient methods, rheology model generalization, boundary conditions, and immersed-boundary method can be accessed in **Appendix B**.

4 Results

In seismic sections, three MTCs are characterized by internally chaotic seismic facies (Figure 2). They are bounded by a continuous high-amplitude basal shear surface and a rugose low-amplitude top surface (Figure 2). These seismic characteristics indicate that three MTCs underwent intensive internal deformation and are categorized as debris-flow type MTCs (Jackson, 2011; Ortiz-Karpf et al., 2017). We pick six horizons defining the bases and tops of three MTCs for seismic attribute and well log analysis (Figure 2).

4.1 MTC-1

Observation: MTC-1 is bounded by horizon H1 at its base and horizon H2 at its top (Figure 2). The lateral and distal boundaries of MTC-1 extend beyond the limits of the 3D seismic dataset. Structure map and variance attribute map from horizon H1 shows a series of E-trending lineations that are generally oriented downslope (Figure 3a & b). These lineations range from 50~100m in width, 2.5~5.0km in length, and exhibit erosional characteristics, cutting downward into the underlying substrate. The central region of MTC-1 contains a block-shaped feature and exhibits a higher-variance boundary compared to the surrounding area (Figures 3a & b). In the correlated seismic section, the block exhibits internally sub-parallel, continuous, high-amplitude seismic reflections (Figure 2). Below the block, the seismic reflections are marked by high-amplitude and negative polarity opposite to the seabed reflection (Figure 2). Within the blocks, pull-up reflections that vertically traverse the block and overlying MTC-1 (Figure 2). These pull-up seismic reflections form pipe like features extending to the seabed, where they generate 200~500m wide depressions on the seabed (Figure 2). The eastern region of MTC-1 shows a continuous SSW-trending scarp (Figure 3a). In the correlated seismic section, the scarp manifests as a segment of the basal shear surface that discordantly cuts up to a stratigraphically higher strata at a high angle (Figure 2). Spectral decomposition attribute extracted from horizon H1 shows a series of concave-eastward, regularly spaced subparallel lineations developed adjacent to the easternmost part of the scarp (Figure 3c). These subparallel lineations appear in seismic section as semicontinuous, medium-amplitude reflections (Figure 2).

Interpretation: The E-trending lineations are interpreted as grooves, forming by clasts entrained within the host flow (e.g., debris flow) that abraded the contemporaneous seabed (Figure 3d; Posamentier and Martinsen, 2011; Sobiesiak et al., 2018). Grooves typically develop parallel to the main flow direction, suggesting that MTC-1 was emplaced in a E-direction (Bull et al., 2009). The block-shaped feature, characterized by internally sub-parallel, continuous seismic reflections, is interpreted as a remnant block, representing an isolated segment of sediment that has not undergone failure (Bull et al., 2009). The high-amplitude negative reflections stacked below the remnant block are interpreted as evidence of gas hydrate presence (BSR 3 in Figure 2; Kuang et al., 2023; Wang et al., 2025). We therefore indicate the formation of remnant block is attributed to gas hydrate cementation, which significantly increases sediment strength and inhibits deformation (Zhao et al., 2023).

The pull-up seismic reflections with pipe-like geometries are interpreted as manifestations of fluid escape structures (Wang et al., 2025). The updip parts of these pipes, which connect to seabed depressions, are interpreted as pockmarks in previous studies and are indicative of recurrent cold seep activity (Ye et al., 2019; Ren et al., 2024; Wang et al., 2025). Considering the spatial correlation between fluid escape structures that crosscut MTC-1, we infer that seal failure has occurred at the location of the remnant block.

The SSW-trending scarp is interpreted as a frontal ramp, formed by the upward incision of the MTCs into shallower stratigraphic levels (Bull et al., 2009). Previous studies indicate that the strata below the frontal ramp are deposited as sandy turbidite complexes (Figure 2; Kuang et al., 2023). The sandy turbidites potentially enhance the mechanical strength thus erosion resistance by raising critical shear stress threshold, thereby promoting the formation of a stepped frontal ramp (Mitchener & Torfs, 1996). The concave-eastward, regularly spaced subparallel lineations are interpreted as pressure ridges, formed by a combination of shear compression and resistance from the undeformed sediments during the deceleration and eventual cessation of MTC movement (Figure 3d; Bull et al., 2009).

4.2 MTCs 2&3

Observation: MTC-2 is bounded by Horizon H3 at its base and Horizon H4 at its top (Figure 2). Its lateral extent surpasses the limits of the available 3D seismic dataset. Variance and spectral decomposition attributes extracted from the basal shear surface (H3) reveal a series of E-trending lineations, morphologically comparable to those on Horizon H1 (Figures 4a–4c). These lineations terminate at the distal edge of MTC-2, defining a distinct boundary that marks the downslope limit of the MTC-2 (Figures 4b & 4c).

MTC-3 is confined between Horizon H5 at the base and Horizon H6 at the top (Figure 2). Its lateral margin extends beyond the 3D seismic dataset. Variance and spectral decomposition attributes from Horizon H5 reveal a basal shear surface characterized by E-trending lineations, ranging from 0.1~2.5

km in width and 2.5~15 km in length (Figure 5a–5c). These E-trending lineations exhibit a divergent pattern downslope, suggesting flow spreading and possible lateral unconfined emplacement (Figure 5c). The termination of these grooves delineates the distal margin of MTC-3, marked by a distinct boundary of seismic striation cessation (Figures 5b & 5c).

A cluster of semi-rounded, crater-like depressions measuring 50~100 m in diameter is observed beyond the distal margins of MTC-2 and MTC-3 (Figures 4b & 5b). In the variance attribute map, they correspond to zones of elevated variance (Figure 6a), while the spectral decomposition map shows scattered bright spots coinciding with their locations (Figure 6b). In seismic sections, the depressions are situated directly above topographic highs associated with frontal ramp beneath MTC-1 (Figures 6c & 6d). They are bounded by near-vertical (~90°) discontinuities but lack internal deformation typically linked to MTCs emplacement, such as folding or faulting.

Interpretation: Consistent with MTC-1, the E-trending lineations on the basal shear surface of MTC-2 and MTC-3 are interpreted as grooves (Figure 4d & 5d; Posamentier and Martinsen, 2011; Sobiesiak et al., 2018). The E-trending erosional features with divergent shape on the basal shear surface of MTC-3 are interpreted as scours, formed when the basal drag is great enough to allow the mass movement to plough into the substrate (Figure 5d; Sobiesiak et al., 2018). Considering the kinematic indicators provided by grooves and scours, the emplacement direction of MTC-2 and MTC-3 is inferred as E-in general.

The semi-rounded, crater-like depressions observed beyond the distal margins of MTC-2 and MTC-3 suggest a post-emplacement origin, likely associated with vertical fluid escape (Figure 6d). Additionally, an exploration well drilled near the fluid escape pipes was halted due to significant influx of methane gas from the borehole, confirming the escaping fluids were methane-bearing (Kuang et al., 2023). The semi-rounded, crater-like depressions are thus interpreted as fluid escape pipes caused by the seepage of methane-bearing fluids (Figure 6d; Cartwright & Santamarina, 2015;

Ye et al., 2019). The presence of fluid escape pipes directly above the frontal ramp of MTC-1 (Figure 6d) suggests that seal failure occurred at the frontal ramp crest.

4.3 MTCs petrophysical properties

Observation: Compared to the overlying and underlying non-MTCs units, MTCs are normally characterized by increased density (1.8~2.0 g/cm³), resistivity (1.3~2.5 Ω·m), and decreased porosity (45~65%), permeability (0.5~6.5 mD), which remains consistent with previously published studies (Figure 7; Dugan, 2012; Sawyer et al., 2009). Within MTC-1, petrophysical properties change sharply across the remnant block and frontal ramp, both of which are topographic highs along the basal shear surface. Above the topographic highs, MTC-1 exhibits lower density (1.6~1.7 g/cm³), lower resistivity (0.7~1.6 Ω·m), and higher porosity (55~80%) and permeability (2.5~10.5 mD) compared to the normal MTC-1 intervals devoid of these features (Figure 8). More specifically, the density of MTC-1 overlying topographic highs is approximately 13% lower than that of flat areas (Figure 8a), while resistivity decreases by ~39% (Figure 8b), porosity increases by ~23% (Figure 8c), and permeability increases by ~217% (Figure 8d).

Interpretation: The significantly lower density and resistivity, coupled with higher porosity and permeability observed above the remnant block and frontal ramp, indicate a substantially reduced degree of compaction over these topographic highs. The reduced compaction above the remnant block and frontal ramp implies that the seal integrity of MTC-1 in these zones is significantly weakened. This is consistent with the fluid escape structures observed within the remnant block and above frontal ramp, suggesting potential vertical fluid migration pathways (Figure 2 & Figure 6). Thus, the seal integrity of MTC-1 exhibits spatial variability, with the areas above the remnant block and frontal ramp showing lower degrees of compaction and potentially reduced seal integrity.

5 Discussions and Implications

5.1 Shear Localization as a Key Control on MTCs Seal Integrity

Previous studies have identified two primary mechanisms responsible for MTC seal failure: (1) faultcontrolled fluid migration, where normal or thrust faults provide permeable pathways for fluid escape (e.g., Pattier et al., 2013; Yang et al., 2013); and (2) overpressure-driven breaching, where MTCs emplacement induces overpressure in underlying strata, triggering upward fluid migration and seal failure (e.g., Moernaut et al., 2017). In this study, the three MTCs exhibit no seismically resolvable internal faulting or folding, and no evidence of overpressure is observed in the underlying gas hydrate system (Kuang et al., 2023), suggesting that neither fault-assisted nor overpressure-driven mechanisms can account for the observed seal failure. The following section investigates the potential triggers of MTCs seal failure in the study area.

We use a two-dimensional numerical solver based on finite difference discretization and implicit pseudo-transient methods to model the distribution and evolution of shear strain during MTCs emplacement (Räss et al., 2022; Trujillo-Vela et al., 2022). Numerical simulation shows that, under conditions of flat basal shear surface with a tilt angle 1.2°, shear strain consistently develops within a 4.0~8.0, representing approximately 10~20% of the total MTC thickness confined to its lowermost part (Figure 9a). This concentration of shear strain is referred to as shear localization, characterized by a distinct deformation band with elevated shear strain rates during MTCs emplacement (Anders et al., 2000; Mitchell et al., 2015; Viesca & Rice, 2012). The presence of shear localization in the lower part of the MTC is consistent with petrophysical and outcrop-based studies, which identify the lowermost 15~30 m, accounting for 10~20% MTC total thickness, similar to the modeled proportion, as the densest interval that accommodated the majority of shear deformation during emplacement (Hodgson et al., 2019; Wu et al., 2021).

As seismic and well log interpretations reveal that seal failure occurs above the remnant block and frontal ramp, we simulate two additional scenarios in which the MTC basal shear surface traverses these topographic features. In the first scenario, as MTC flows over a frontal ramp, shear strain intensifies along the ramp edge, while it decreases across the ramp crest (Figure 9b). In the second scenario, as the MTC overrides a remnant block, shear strain is elevated along the margins of the basal shear surface adjacent to the block, while it is markedly reduced across the flat upper surface of the block (Figure 9c). These results indicate that as MTCs traverse structures containing positive relief, such as frontal ramps and remnant blocks, the localization of basal shear strain is disrupted, which leads to a decline in shear intensity and a disrupt in the basal shear zone's integrity. This in turn explains the petrophysical observations that MTC intervals above the topographic highs exhibit lower density and resistivity along with higher porosity and permeability, which establishes reduced compaction due to disrupted shear localization as the ultimate cause of MTCs seal failure.

Shear strain plays a key role in shaping the microstructure of granular materials, while shear localization influences the spatial distribution of shear strain. High shear strain promotes grain size reduction (Mitchell et al., 2015; Siman-Tov & Brodsky, 2018), collapse of pore bodies (Emmanuel & Day-Stirrat, 2012) and realignment of pore throats (Kanamatsu et al., 2014; Roy et al., 2022; Wang et al., 2020), which collectively reduce permeability and enhance seal integrity (Cardona et al., 2022). In contrast, low shear strain suppresses these effects, allowing partial recovery of pore structures and widening of seepage pathways due to elastic rebound (Zhao et al., 2023). This reduced compaction weakens seal integrity and facilitates fluid escape.

In this work, we demonstrate that MTCs seal integrity is primarily controlled by basal topographic variations as they influence the distribution of shear strain through shear localization (Figure 10a). Topographic highs can disrupt the continuity of the shearing and generate localized zones of low shear strain in MTCs. These low-strain regions trigger elastic rebound and limit grain size segregation, which together widen seepage pathways and increase permeability, ultimately weakening the seal integrity of MTCs above such features (Figure 10b). In contrast, flat topography or the margins of topographic highs tend to concentrate shear strain, promoting grain size reduction, pore-throat collapse, and directional pore alignment. These processes restrict fluid migration and enhance the seal integrity of MTCs in these zones (Figure 10c; Gatter et al., 2021).

5.2 Implications for gas hydrate formation and distribution

BSRs in the study area exhibit distinct fluid migration and hydrate formation characteristics, each influenced by the sealing behavior of MTC-1. In regions where MTC-1 maintains an intact basal shear zone (i.e., lacking remnant blocks and frontal ramp), it exhibits strong seal integrity, allowing methane-rich fluids sourced from the Songnan Low Uplift to accumulate beneath the MTC and thus forming BSR 1 (Table 2; Figure 11; Kuang et al., 2023). The free gas associated with BSR 1 subsequently migrates laterally, serving as the methane source for the formation of both BSR 2 and BSR 3 (Figure 11).

BSR 2 lies beneath an area where MTC-1 also lacks topographic highs and maintains strong seal integrity. The strong seal integrity promotes high-pressure and low-temperature conditions, under which gas hydrate tends to crystallize from methane-rich fluids (Sloan, 2003; Walsh et al., 2009; Crutchley et al., 2014) and eventually leads to the formation of high-saturation gas hydrates in BSR 2 (Table 2; Figure 11). However, upon reaching the crest of frontal ramp, where the seal integrity of MTC-1 is compromised, methane-rich fluids are able to migrate vertically. This upward migration penetrates the under-compacted zones in MTC-1 and the overlying MTCs 2&3, resulting in the formation of crater-like pockmarks that serve as geomorphic evidence of focused fluid escape (Figure 11).

In contrast, BSR 3 lies beneath an area where MTC-1 contains a remnant block and exhibits compromised seal integrity (Figure 11). The weakened seal promotes moderate-pressure and low-temperature conditions, under which methane-rich fluids partially crystallize to gas hydrate during advection and partially remain as free gas (Ker et al., 2019; Milkov et al., 2004; Ruppel & Kessler, 2017). This leads to the formation of the low-saturation gas hydrates that coexist with free gas in BSR 3 (Table 2; Figure 11). The remained free gas subsequently ascends through the under-compacted zones overlying remnant block and eventually breaches the seabed, forming a cluster of pockmarks (Figure 11).

Thus, we demonstrate that the seal integrity of MTCs fundamentally controls fluid migration and hydrate accumulation modes. When MTCs exhibit intact basal shear zone (e.g., lacking frontal ramp or remnant block), they act as effective seals and promote lateral fluid migration, allowing free gas reservoirs (e.g., BSR 1) or high-saturation hydrates (e.g., BSR 2) to form under respectively favorable pressure-temperature conditions. In contrast, when MTCs exhibit disrupted basal shear zone (e.g., containing frontal ramp or remnant block), the seal integrity of MTCs is compromised. The free gas may migrate vertically through these zones with compromised seal integrity, forming pockmarks when gas supply is limited or coexisting free gas and low-saturation gas hydrates (e.g., BSR 3) when gas supply is sufficient. Therefore, the spatial variability in MTCs seal integrity controls fluid migration pathways, directly governing gas hydrate formation and distribution.

6 Conclusions

In this study, we integrate 3D seismic reflection and well log data to investigate the sealing behavior of three vertically stacked MTCs in the Qiongdongnan Basin, northern South China Sea, with the aim of identifying the key factors that control their seal integrity. We show that:

(1) Shear localization consistently develops in the lowermost part of MTCs during emplacement, forming a narrow, highly deformed basal shear zone. This shear-focused deformation enhances compaction, reduces porosity and permeability, and is therefore critical for the seal integrity of MTCs.

(2) Topographic highs on basal shear surface such as frontal ramps and remnant blocks can disturb shear localization by reducing localized shear strain. This disruption results in lower degrees of compaction and higher permeability above these topographic highs, ultimately leading to localized seal failure.

(3) Shear localization plays a key role in focusing fluid escape and thus governs the spatial distribution and accumulation of gas hydrates. Intact MTC seals promote free gas or high-saturation hydrate accumulation, whereas compromised seals result in low-saturation hydrates coexisting with free gas.

(4) Understanding the conditions under which MTCs function as effective seals, or fail, is crucial for predicting gas hydrate distribution and identifying suitable sites for subsea carbon dioxide storage in submarine settings. Therefore, such knowledge of subsurface fluid flow is critical for derisking future hydrocarbon exploration and carbon dioxide storage initiatives.

Appendix A: Seismic well tie

We show one example of seismic-well tie using W1 (Figure A1). Here, sonic and density logs are used to generate synthetic seismograms:

$$Reflection = \frac{\rho_2 v_2 - \rho_1 v_1}{\rho_2 v_2 + \rho_1 v_1} \tag{A1}$$

where ρ is density $[kg \cdot m^{-3}]$, v is P-wave velocity $[m \cdot s^{-1}]$, and the subscripts denote two subsurface layers.

The set of reflection coefficients is then band limited to the same frequency band as the actual seismic data (Lines & Newrick, 2004). Between the well log synthetic seismograms and actual seismic data, correlations are made through the vertical stretch or squeeze of the seismograms to match key subsurface intervals. Finally, the relationship between depth domain well log data and time domain seismic data can be established.

Appendix B: Numerical modelling

B1. Implicit pseudo-transient methods

The implicit pseudo-transient method is a powerful numerical technique renowned for its robustness in tackling strongly nonlinear problems, such as shear band formation in visco-elasto-plastic media (Räss et al., 2022). This iterative approach enhances stability in the solution process by introducing a pseudo-time derivative, making it highly effective for modeling complex rheological behaviors (Räss et al., 2022). Studies have shown it can deliver over 96% parallel efficiency on distributed-memory systems utilizing up to 2197 graphics processing units (Räss et al., 2022). Under these circumstances, implicit pseudo-transient method possesses high robustness and scalability, which makes it well suited for solving the momentum equation to approximate the shear deformation within MTCs.

At each physical time step, implicit pseudo-transient method is implemented for the iterative solution to the momentum equation:

$$\frac{\partial p}{\partial \Gamma_p} = -\frac{\partial u_i}{\partial x_i} \tag{B1}$$

$$\frac{\partial u_i}{\partial \Gamma_u} = \frac{\partial \tau_{ij}}{\partial x_j} - \frac{\partial p}{\partial x_i} + F_i - \rho\left(u_j \frac{\partial u_i}{\partial x_j}\right) \tag{B2}$$

where Γ presents the pseudo-time step.

An implicit solution of the momentum equations can be achieved when the continuity residual $\frac{\partial p}{\partial \Gamma_p}$ and the momentum residual $\frac{\partial u_i}{\partial \Gamma_u}$ are minimized. The detailed implementation processes of implicit pseudo-transient methods can be found in Räss et al. (2022).

B2. Herschel-Bulkley rheology model

The generalized rheology model for simple shear is implemented using:

$$\tau_{ij} = \tau_0 + k_0 \dot{\varepsilon}_{ij}^n \tag{B3}$$

$$\left|\frac{\dot{\varepsilon}_{ij}}{\dot{\varepsilon}_r}\right|^n = \mathrm{sgn}(\dot{\varepsilon}_{ij})\frac{\tau_{ij}}{\tau_0} - 1 \tag{B4}$$

where τ_0 is the yield shear stress $[Pa]$, k_0 is the consistency index $[Pa \cdot s^n]$, n is the flow index $[dimensionless]$, $\dot{\varepsilon}_{ij}$ is the strain rate tensor $[s^{-1}]$, given as:

$$\dot{\varepsilon}_{ij} = \sqrt{\frac{1}{2}\tau_{ij}\tau_{ij}} \tag{B5}$$

$\dot{\varepsilon}_r$ is the reference strain rate $[s^{-1}]$, given as:

$$\dot{\varepsilon}_r = \left(\frac{\tau_0}{k_0}\right)^{\frac{1}{n}} \tag{B6}$$

The detailed implementation processes can be found in Zafar et al. (2024).

B3. Outlet boundary conditions

We adopt the outlet boundary condition from Orlanski (1976). This boundary condition allows phenomena generated in the domain of interest to pass through the boundary without undergoing significant distortion or influencing the interior solution, and it is an optimal solution for balancing accuracy and efficiency.

$$\frac{\partial u}{\partial t} + U\frac{\partial u}{\partial x} = 0 \tag{B7}$$

From Kreiss (1968) and Gustafsson et al. (1972), the propagation speed U is numerically estimated by $U = \frac{\Delta x}{\Delta t}$, where Δx and Δt are the spatial and temporal grid sizes. The speed at the outlet boundary is then as follows:

$$u_{n_x}^{n_t} = 2u_{n_{x-1}}^{n_{t-1}} - u_{n_{x-2}}^{n_{t-2}} \tag{B8}$$

where n_x is the boundary point and n_t is the current time step.

B4. Immersed-boundary method

Immersed-boundary method is used to prescribe the fictitious interface between MTCs and undeformed strata. The general idea is using both Eulerian and Lagrangian approaches to solve the governing equations on the MTC domain with a correction on the interface between MTCs and undeformed strata (Zhao et al., 2021). Lagrangian approach describes fluid motion focusing on an individual fluid parcel as it moves through space and time, while Eulerian approach describes fluid motion focusing on specific locations in the space through which the fluid flows as time passes (Peskin, 1972, 2002). The interface (the immersed boundary) is represented independently as a set of discrete points (Lagrangian variables) that define its shape and position (Peskin, 1972, 2002). This interface cuts through the MTC domain grid (Eulerian variables), which is the fixed grid where the governing equations are solved (Peskin, 1972, 2002). This method avoids the computationally expensive and often challenging task of generating and deforming body-conforming meshes for intricate or rapidly moving boundaries (e.g. basal shear surface). The detailed implementation processes of the immersed-boundary method can be found in Zhao et al. (2021) and Liu et al. (2024).

Appendix C: Gas hydrate saturation estimation

To determine the actual formations of multiple amplitude anomalies in seismic data, gas hydrate saturation is calculated using Archie's porosity-resistivity equation and saturation equation (Archie, 1942):

$$S_h = 1 - \left(\frac{R_0}{R_m}\right)^{\frac{1}{n_{Archie}}}, \qquad R_0 = \frac{R_w}{\phi^m} \tag{C1}$$

where S_h $[m^3 \cdot ms^{-3}]$ is the gas hydrate saturation, R_0 $[\Omega_m]$ is the background resistivity, R_m $[\Omega_m]$ is the measured resistivity, n_{Arch} $[dimensionless]$ is Archie's saturation exponent (set equal to 2.5 according to Cook and Waite, 2018), R_w $[\Omega_m]$ is the pore water resistivity (set equal to $0.3\Omega_m$ according to the resistivity of seawater), m is the cementation exponent (set equal to 2 according to Cook et al., 2023).

Acknowledgments

We thank the Guangzhou Marine Geological Survey for providing seismic and well log data and for granting permission to publish this work. This research was supported by the National Key Research and Development Program of China (Grant No. 2021YFC2800901). The corresponding author also acknowledges financial support from the National Natural Science Foundation of China (Grant No.

42406060), the Natural Science Foundation of Shanghai (Grant No. 23ZR1467800), and the Fundamental Research Funds for the Central Universities, China.

Data Availability Statement

The 3D seismic and well log data were obtained from a series of proprietary surveys conducted by the Guangzhou Marine Geological Survey in 2018, 2021 and 2022 for the gas hydrate exploration. These data, uploaded by Kuang et al. (2023), are available in the Zenodo repository (https://doi.org/10.5281/zenodo.7721790). The codes used for numerical simulations are available in the Zenodo repository (https://zenodo.org/records/16252096). Requests for datasets can be made through Guangzhou Marine Geological Survey via the corresponding author.

References

Alves, T. M., & Cartwright, J. A. (2010). The effect of mass-transport deposits on the younger slope morphology, offshore Brazil. *Marine and Petroleum Geology*, *27*(9), 2027–2036. https://doi.org/10.1016/j.marpetgeo.2010.05.006

Alves, T. M., Kurtev, K., Moore, G. F., & Strasser, M. (2014). Assessing the internal character, reservoir potential, and seal competence of mass-transport deposits using seismic texture: A geophysical and petrophysical approach. *AAPG Bulletin*, *98*(4), 793–824. https://doi.org/10.1306/09121313117

Anders, M. H., Aharonov, E., & Walsh, J. J. (2000). Stratified granular media beneath large slide blocks: Implications for mode of emplacement. *Geology*, *28*(11), 971–974. https://doi.org/10.1130/0091-7613(2000)28<971:SGMBLS>2.0.CO;2

Anomneze, D. O., Oguadinma, V. O., Ayodele, I. J., & Ajaegwu, N. E. (2025). Application of iso-frequency extractions and spectral frequency blending in hydrocarbon delineation of thin-pay and thick-pay reservoirs, Niger Delta Basin. *Energy Geoscience*, *6*(2), 100396. https://doi.org/10.1016/j.engeos.2025.100396

Archie, G. E. (1942). The Electrical Resistivity Log as an Aid in Determining Some Reservoir Characteristics. *Transactions of the AIME*, *146*(01), 54–62. https://doi.org/10.2118/942054-G

Bataller, F. J., McDougall, N., & Moscariello, A. (2019). Ordovician glacial paleogeography: Integration of seismic spectral decomposition, well sedimentological data, and glacial modern analogs in the Murzuq Basin, Libya. *Interpretation*, *7*(2), T383–T408. https://doi.org/10.1190/INT-2018-0069.1

Bull, S., Cartwright, J., & Huuse, M. (2009). A review of kinematic indicators from mass-transport complexes using 3D seismic data. *Marine and Petroleum Geology*, 26(7), 1132–1151. https://doi.org/10.1016/j.marpetgeo.2008.09.011

Cardona, S., Kobayashi, H., Wood, L., Dugan, B., & Milkov, A. V. (2022). Assessing the sealing quality of submarine mass transport complexes and deposits. *Marine and Petroleum Geology*, 143, 105748. https://doi.org/10.1016/j.marpetgeo.2022.105748

Cartwright, J., Huuse, M., & Aplin, A. (2007). Seal bypass systems. *AAPG bulletin*, *91*(8), 1141-1166.

Cartwright, J., & Santamarina, C. (2015). Seismic characteristics of fluid escape pipes in sedimentary basins: Implications for pipe genesis. *Marine and Petroleum Geology*, *65*, 126-140.

Chang, Y.-C., Mitchell, N. C., & Quartau, R. (2021). Landslides in the Upper Submarine Slopes of Volcanic Islands: The Central Azores. *Geochemistry, Geophysics, Geosystems*, *22*(10), e2021GC009833. https://doi.org/10.1029/2021GC009833

Chapp, E., Taylor, B., Oakley, A., & Moore, G. F. (2008). A seismic stratigraphic analysis of Mariana forearc basin evolution. *Geochemistry, Geophysics, Geosystems*, *9*(10). https://doi.org/10.1029/2008GC001998

Chen, D., Zhang, G., Dong, D., Zhao, M., & Wang, X. (2022). Widespread Fluid Seepage Related to Buried Submarine Landslide Deposits in the Northwestern South China Sea. *Geophysical Research Letters*, *49*(6), e2021GL096584. https://doi.org/10.1029/2021GL096584

Chopra, S., & Marfurt, K. J. (2007). *Seismic Attributes for Prospect Identification and Reservoir Characterization*. Society of Exploration Geophysicists and European Association of Geoscientists and Engineers. https://doi.org/10.1190/1.9781560801900

Cook, A. E., Portnov, A., Heber, R. C., Vadakkepuliyambatta, S., & Bünz, S. (2023). Widespread subseafloor gas hydrate in the Barents Sea and Norwegian Margin. *Earth and Planetary Science Letters*, *604*, 117993. https://doi.org/10.1016/j.epsl.2023.117993

Cook, A. E., & Waite, W. F. (2018). Archie's Saturation Exponent for Natural Gas Hydrate in Coarse-Grained Reservoirs. *Journal of Geophysical Research: Solid Earth*, *123*(3), 2069–2089. https://doi.org/10.1002/2017JB015138

Crutchley, G. J., Klaeschen, D., Planert, L., Bialas, J., Berndt, C., Papenberg, C., Hensen, C., Hornbach, M. J., Krastel, S., & Brueckmann, W. (2014). The impact of fluid advection on gas hydrate stability: Investigations at sites of methane seepage offshore Costa Rica. *Earth and Planetary Science Letters*, 401, 95–109. https://doi.org/10.1016/j.epsl.2014.05.045

Daigle, H., & Dugan, B. (2009). Extending NMR data for permeability estimation in fine-grained sediments. *Marine and Petroleum Geology,* *26*(8), 1419–1427. https://doi.org/10.1016/j.marpetgeo.2009.02.008

Day-Stirrat, R. J., Flemings, P. B., You, Y., & van der Pluijm, B. A. (2013). Modification of mudstone fabric and pore structure as a result of slope failure: Ursa Basin, Gulf of Mexico. *Marine Geology*, *341*, 58–67. https://doi.org/10.1016/j.margeo.2013.05.003

Dugan, B. (2012). Petrophysical and consolidation behavior of mass transport deposits from the northern Gulf of Mexico, IODP Expedition 308. *Marine Geology, 315–318*, 98–107. https://doi.org/10.1016/j.margeo.2012.05.001

Gatter, R., Clare, M. A., Kuhlmann, J., & Huhn, K. (2021). Characterisation of weak layers, physical controls on their global distribution and their role in submarine landslide formation. *Earth-Science Reviews*, *223*, 103845. https://doi.org/10.1016/j.earscirev.2021.103845

Gustafsson, B., Kreiss, H.-O., & Sundström, A. (1972). Stability Theory of Difference Approximations for Mixed Initial Boundary Value Problems. II. *Mathematics of Computation*, *26*(119), 649–686. https://doi.org/10.2307/2005093

Eckersley, A. J., Lowell, J., & Szafian, P. (2018). High-definition frequency decomposition. *Geophysical Prospecting*, *66*(6), 1138–1143. https://doi.org/10.1111/1365-2478.12642

Emmanuel, S., & Day-Stirrat, R. J. (2012). A framework for quantifying size dependent deformation of nano-scale pores in mudrocks. *Journal of Applied Geophysics*, *86*, 29–35. https://doi.org/10.1016/j.jappgeo.2012.07.011

Han, Z. (2025). Shear localization as a key control on mass-transport complexes seal integrity: insights from geophysical datasets [Dataset]. *Zenodo.* https://zenodo.org/records/16252096

Hodgson, D. M., Brooks, H. L., Ortiz-Karpf, A., Spychala, Y., Lee, D. R., & Jackson, C. A.-L. (2019). Entrainment and abrasion of megaclasts during submarine landsliding and their impact on flow behaviour. *Geological Society, London, Special Publications*, *477*(1), 223–240. https://doi.org/10.1144/SP477.26

Huang, B., Tian, H., Li, X., Wang, Z., & Xiao, X. (2016). Geochemistry, origin and accumulation of natural gases in the deepwater area of the Qiongdongnan Basin, South China Sea. *Marine and Petroleum Geology*, *72*, 254–267. https://doi.org/10.1016/j.marpetgeo.2016.02.007

Hunt, J. E., Wynn, R. B., Talling, P. J., & Masson, D. G. (2013). Turbidite record of frequency and source of large volume (>100 km3) Canary Island landslides in the last 1.5 Ma: Implications for landslide triggers and geohazards. *Geochemistry, Geophysics, Geosystems*, *14*(7), 2100–2123. https://doi.org/10.1002/ggge.20139

Hustoft, S., Dugan, B., & Mienert, J. (2009). Effects of rapid sedimentation on developing the Nyegga pockmark field: Constraints from hydrological modeling and 3-D seismic data, offshore mid-Norway. *Geochemistry, Geophysics, Geosystems*, *10*(6). https://doi.org/10.1029/2009GC002409

Iverson, R. M. (1997). The physics of debris flows. *Reviews of Geophysics, 35*(3), 245–296. https://doi.org/10.1029/97RG00426

Jackson, C. A.-L. (2011). Three-dimensional seismic analysis of megaclast deformation within a mass transport deposit; implications for debris flow kinematics. *Geology*, *39*(3), 203–206. https://doi.org/10.1130/G31767.1

Kanamatsu, T., Kawamura, K., Strasser, M., Novak, B., & Kitamura, Y. (2014). Flow dynamics of Nankai Trough submarine landslide inferred from internal deformation using magnetic fabric. *Geochemistry, Geophysics, Geosystems*, *15*(10), 4079–4092. https://doi.org/10.1002/2014GC005409

Karstens, J., Haflidason, H., Berndt, C., & Crutchley, G. J. (2023). Revised Storegga Slide reconstruction reveals two major submarine landslides 12,000 years apart. *Communications Earth & Environment*, *4*(1), 1–9. https://doi.org/10.1038/s43247-023-00710-y

Kenyon, W. E., Day, P. I., Straley, C., & Willemsen, J. F. (1988). A three-part study of NMR longitudinal relaxation properties of water-saturated sandstones. *SPE formation evaluation, 3*(03), 622-636.

Ker, S., Thomas, Y., Riboulot, V., Sultan, N., Bernard, C., Scalabrin, C., Ion, G., & Marsset, B. (2019). Anomalously Deep BSR Related to a Transient State of the Gas Hydrate System in the Western Black Sea. *Geochemistry, Geophysics, Geosystems*, *20*(1), 442–459. https://doi.org/10.1029/2018GC007861

Kreiss, H.-O. (1968). Stability Theory for Difference Approximations of Mixed Initial Boundary Value Problems. I. *Mathematics of Computation*, *22*(104), 703–714. https://doi.org/10.2307/2004572

Kuang, Z., Cook, A., Ren, J., Deng, W., Cao, Y., & Cai, H. (2023). A Flat-Lying Transitional Free Gas to Gas Hydrate System in a Sand Layer in the Qiongdongnan Basin of the South China Sea. *Geophysical Research Letters, 50*(24), e2023GL105744. https://doi.org/10.1029/2023GL105744

Kuang, Z., Cook, A., Ren, J., Deng, W., Cao, Y., & Cai, H. (2023). A flat-lying transitional free gas to gas hydrate system in a sand layer in the Qiongdongnan Basin of the South China Sea [Dataset]. *Zenodo.* https://doi.org/10.5281/zenodo.7721790

Lastras, G., Canals, M., Urgeles, R., Hughes-Clarke, J. E., & Acosta, J. (2004). Shallow slides and pockmark swarms in the Eivissa Channel, western Mediterranean Sea. *Sedimentology*, *51*(4), 837-850.

Lines, L. R., & Newrick, R. T. (2004). *Fundamentals of geophysical interpretation*. Society of Exploration Geophysicists.

Liu, E. W., Räss, L., Herman, F., Podladchikov, Y., & Suckale, J. (2024). Spontaneous Formation of an Internal Shear Band in Ice Flowing Over Topographically Variable Bedrock. *Journal of Geophysical Research: Earth Surface, 129*(4), e2022JF007040. https://doi.org/10.1029/2022JF007040

Milkov, A. V., Dickens, G. R., Claypool, G. E., Lee, Y.-J., Borowski, W. S., Torres, M. E., Xu, W., Tomaru, H., Tréhu, A. M., & Schultheiss, P. (2004). Co-existence of gas hydrate, free gas, and brine within the regional gas hydrate stability zone at Hydrate Ridge (Oregon margin): Evidence from prolonged degassing of a pressurized core. *Earth and Planetary Science Letters, 222*(3), 829–843. https://doi.org/10.1016/j.epsl.2004.03.028

Mitchell, T. M., Smith, S. A. F., Anders, M. H., Di Toro, G., Nielsen, S., Cavallo, A., & Beard, A. D. (2015). Catastrophic emplacement of giant landslides aided by thermal decomposition: Heart Mountain, Wyoming. *Earth and Planetary Science Letters*, *411*, 199–207. https://doi.org/10.1016/j.epsl.2014.10.051

Mitchener, H., & Torfs, H. (1996). Erosion of mud/sand mixtures. *Coastal Engineering*, *29*(1), 1–25. https://doi.org/10.1016/S0378-3839(96)00002-6

Moernaut, J., Wiemer, G., Reusch, A., Stark, N., De Batist, M., Urrutia, R., Ladrón de Guevara, B., Kopf, A., & Strasser, M. (2017). The influence of overpressure and focused fluid flow on subaquatic slope stability in a formerly glaciated basin: Lake Villarrica (South-Central Chile). *Marine Geology*, *383*, 35–54. https://doi.org/10.1016/j.margeo.2016.11.012

Mountjoy, J. J., Pecher, I., Henrys, S., Crutchley, G., Barnes, P. M., & Plaza-Faverola, A. (2014). Shallow methane hydrate system controls ongoing, downslope sediment transport in a low-velocity active submarine landslide complex, Hikurangi Margin, New Zealand. *Geochemistry, Geophysics, Geosystems, 15*(11), 4137–4156. https://doi.org/10.1002/2014GC005379

Noda, A., TuZino, T., Joshima, M., & Goto, S. (2013). Mass transport-dominated sedimentation in a foreland basin, the Hidaka Trough, northern Japan. *Geochemistry, Geophysics, Geosystems*, *14*(8), 2638–2660. https://doi.org/10.1002/ggge.20169

Orlanski, I. (1976). A simple boundary condition for unbounded hyperbolic flows. *Journal of computational physics*, *21*(3), 251-269.

Ortiz-Karpf, A., Hodgson, D. M., Jackson, C. A.-L., & McCaffrey, William. D. (2017). Influence of Seabed Morphology and Substrate Composition On Mass-Transport Flow Processes and Pathways: Insights From the Magdalena Fan, Offshore Colombia. *Journal of Sedimentary Research*, *87*(3), 189–209. https://doi.org/10.2110/jsr.2017.10

Pattier, F., Loncke, L., Gaullier, V., Basile, C., Maillard, A., Imbert, P., Roest, W. R., Vendeville, B. C., Patriat, M., & Loubrieu, B. (2013). Mass-transport deposits and fluid venting in a transform margin setting, the eastern Demerara Plateau (French Guiana). *Marine and Petroleum Geology*, *46*, 287–303. https://doi.org/10.1016/j.marpetgeo.2013.06.010

Peskin, C. S. (1972). Flow patterns around heart valves: a numerical method. *Journal of computational physics*, *10*(2), 252-271.

Peskin, C. S. (2002). The immersed boundary method. *Acta numerica*, *11*, 479-517.

Posamentier, H. W., & Martinsen, O. J. (2011). The character and genesis of submarine mass-transport deposits: insights from outcrop and 3D seismic data. Mass-transport deposits in deepwater settings. *Society for Sedimentary Geology (SEPM) Special Publication, 96*, 7-38.

Räss, L., Utkin, I., Duretz, T., Omlin, S., & Podladchikov, Y. Y. (2022). Assessing the robustness and scalability of the accelerated pseudo-transient method. *Geoscientific Model Development*, *15*(14), 5757–5786. https://doi.org/10.5194/gmd-15-5757-2022

Ren, J., Qiu, H., Kuang, Z., Li, T., He, Y., Xu, M., Wang, X., Lai, H., & Liang, J. (2024). Deep-large faults controlling on the distribution of the venting gas hydrate system in the middle of the Qiongdongnan Basin, South China Sea. *China Geology, 7*(1), 36–50. https://doi.org/10.31035/cg2023086

Roy, N., Frost, J. D., & Viggiani, G. (2022). Pore space evolution of granular assemblies under shear: An experimental study using X-ray tomography. *Granular Matter, 24*(2), 63.

Ruppel, C. D., & Kessler, J. D. (2017). The interaction of climate change and methane hydrates. *Reviews of Geophysics, 55*(1), 126–168. https://doi.org/10.1002/2016RG000534

Sager, T. F., Urlaub, M., Kaminski, P., Papenberg, C., Lastras, G., Canals, M., & Berndt, C. (2022). Development and Emplacement of Ana Slide, Eivissa Channel, Western Mediterranean Sea. *Geochemistry, Geophysics, Geosystems*, *23*(11), e2022GC010469. https://doi.org/10.1029/2022GC010469

Sawyer, D. E., Flemings, P. B., Dugan, B., & Germaine, J. T. (2009). Retrogressive failures recorded in mass transport deposits in the Ursa Basin, Northern Gulf of Mexico. *Journal of Geophysical Research: Solid Earth*, *114*(B10). https://doi.org/10.1029/2008JB006159

Schowalter, T. T. (1979). Mechanics of secondary hydrocarbon migration and entrapment. *AAPG bulletin*, *63*(5), 723-760.

Serov, P., Mattingsdal, R., Winsborrow, M., Patton, H., & Andreassen, K. (2023). Widespread natural methane and oil leakage from sub-marine Arctic reservoirs. *Nature Communications*, *14*(1), 1782. https://doi.org/10.1038/s41467-023-37514-9

Siman-Tov, S., & Brodsky, E. E. (2018). Gravity-Independent Grain Size Segregation in Experimental Granular Shear Flows as a Mechanism of Layer Formation. *Geophysical Research Letters, 45*(16), 8136–8144. https://doi.org/10.1029/2018GL078486

Sloan, E. D. (2003). Fundamental principles and applications of natural gas hydrates. *Nature*, 426(6964), 353–359. https://doi.org/10.1038/nature02135

Sobiesiak, M. S., Kneller, B., Alsop, G. I., & Milana, J. P. (2018). Styles of basal interaction beneath mass transport deposits. *Marine and Petroleum Geology, 98*, 629–639. https://doi.org/10.1016/j.marpetgeo.2018.08.028

Su, M., Wu, C., Chen, H., Li, D., Jiang, T., Xie, X., Jiao, H., Wang, Z., & Sun, X. (2019). Late Miocene provenance evolution at the head of Central Canyon in the Qiongdongnan Basin, Northern South China Sea. *Marine and Petroleum Geology*, *110*, 787–796. https://doi.org/10.1016/j.marpetgeo.2019.07.053

Talling, P. J., Wynn, R. B., Masson, D. G., Frenz, M., Cronin, B. T., Schiebel, R., Akhmetzhanov, A. M., Dallmeier-Tiessen, S., Benetti, S., Weaver, P. P. E., Georgiopoulou, A., Zühlsdorff, C., & Amy, L. A. (2007). Onset of submarine debris flow deposition far from original giant landslide. *Nature, 450*(7169), 541–544. https://doi.org/10.1038/nature06313

Trujillo-Vela, M. G., Ramos-Cañón, A. M., Escobar-Vargas, J. A., & Galindo-Torres, S. A. (2022). An overview of debris-flow mathematical modelling. *Earth-Science Reviews*, *232*, 104135. https://doi.org/10.1016/j.earscirev.2022.104135

Viesca, R. C., & Rice, J. R. (2012). Nucleation of slip-weakening rupture instability in landslides by localized increase of pore pressure. *Journal of Geophysical Research: Solid Earth*, *117*(B3).

Walsh, M. R., Koh, C. A., Sloan, E. D., Sum, A. K., & Wu, D. T. (2009). Microsecond Simulations of Spontaneous Methane Hydrate Nucleation and Growth. *Science, 326*(5956), 1095–1098. https://doi.org/10.1126/science.1174010

Walton, M. A. L., Conrad, J. E., Papesh, A. G., Brothers, D. S., Kluesner, J. W., McGann, M., & Dartnell, P. (2024). A Comprehensive Assessment of Submarine Landslides and Mass Wasting Processes Offshore Southern California. *Geochemistry, Geophysics, Geosystems*, *25*(3), e2023GC011258. https://doi.org/10.1029/2023GC011258

Wang, X., Wang, W., Jin, J., Zhang, G., Luan, Z., Li, C., Wang, M., Zhang, Z., Liu, B., Li, W., & Li, S. (2025). Multiple observations to delineate the characteristics of cold seep system in the Qiongdongnan Basin. *Marine and Petroleum Geology*, *181*, 107522. https://doi.org/10.1016/j.marpetgeo.2025.107522

Wang, Y., Wang, Y., & Zhang, J. (2020). Connecting shear localization with the long-range correlated polarized stress fields in granular materials. *Nature Communications*, *11*(1), 4349. https://doi.org/10.1038/s41467-020-18217-x

Wu, N., Jackson, C. A.-L., Johnson, H. D., & Hodgson, D. M. (2021). Lithological, petrophysical, and seal properties of mass-transport complexes, northern Gulf of Mexico. *AAPG Bulletin, 105*(7), 1461–1489. https://doi.org/10.1306/06242019056

Yang, G., Yin, H., Gan, J., Wang, W., Zhu, J., Jia, D., Xiong, X., & Xu, W. (2022). Explaining structural difference between the eastern and western zones of the Qiongdongnan Basin, northern South China Sea: Insights from scaled physical models. *Tectonics*, *41*(2), e2021TC006899.

Yang, J., Davies, R. J., & Huuse, M. (2013). Gas migration below gas hydrates controlled by mass transport complexes, offshore Mauritania. *Marine and Petroleum Geology, 48*, 366–378. https://doi.org/10.1016/j.marpetgeo.2013.09.003

Ye, J., Wei, J., Liang, J., Lu, J., Lu, H., & Zhang, W. (2019). Complex gas hydrate system in a gas chimney, South China Sea. *Marine and Petroleum Geology*, *104*, 29–39. https://doi.org/10.1016/j.marpetgeo.2019.03.023

Zafar, M. N., Dutykh, D., Sabatier, P., Banjan, M., & Kim, J. (2024). Numerical Reconstruction of Landslide Paleotsunami Using Geological Records in Alpine Lake Aiguebelette. *Journal of Geophysical Research: Solid Earth*, *129*(5), e2023JB028629. https://doi.org/10.1029/2023JB028629

Zhao, E., Dong, Y., Tang, Y., & Cui, L. (2021). Numerical study on hydrodynamic load and vibration of pipeline exerted by submarine debris flow. *Ocean Engineering*, *239*, 109754. https://doi.org/10.1016/j.oceaneng.2021.109754

Zhao, Y., Liu, J., Sang, S., Hua, L., Kong, L., Zeng, Z., & Yuan, Q. (2023). Experimental investigation on the permeability characteristics of methane hydrate-bearing clayey-silty sediments considering various factors. *Energy, 269*, 126811. https://doi.org/10.1016/j.energy.2023.126811

Table and Figure Captions

Table 1. Parameters and corresponding values for numerical simulation.

Table 2. Petrophysical properties of BSRs and associated interpretations.

Figure 1. (a) Overview map of the South China Sea showing the boundary of the Qiongdongnan Basin (red polygon). The black box indicates the extent of figure 1b. The arrows indicate the sediment transport directions. (b) Structural units of the Qiongdongnan Basin with locations of the 3D seismic surveys and well log data.

Figure 2. Perspective view of seismic volume with cross-wells section A-A’ (See Figure 1b for location). The upper surface of the seismic volume is shown as a horizon slice 25ms downwards from seismic horizon H1.

Figure 3. (a) Structure map of Horizon H1 illustrating the basal shear surface of MTC-1. (b) Variance attribute extracted along Horizon H1, showing the grooves, remnant block, frontal ramp. (c) Spectral decomposition and associated frequency attribute extracted along Horizon H1, showing the pressure ridges. RGB Blending is applied as 45Hz, 50Hz, and 60Hz. (d) Interpreted sketch of MTC-1, showing its key kinematic indicators and transport direction.

Figure 4. (a) Structure map of Horizon H3 illustrating the basal shear surface of MTC-2. (b) Variance attribute extracted along the surface 10ms above Horizon H3, showing the grooves, fluid escape pipes, and boundaries of the MTC-2. (c) Spectral decomposition and associated frequency attributes extracted along Horizon H3, showing the grooves, and boundaries of MTC-2. RGB Blending is applied as 40Hz, 50Hz, and 60Hz. (d) Interpreted sketch of MTC-2, showing its boundaries, key kinematic indicators, and transport direction.

Figure 5. (a) Structure map of Horizon H5 illustrating the basal shear surface of MTC-3. (b) Variance attribute extracted along the surface 25ms above Horizon H5, showing the grooves, scours, fluid

escape pipes, and boundaries of MTC-3. (c) Spectral decomposition and associated frequency attributes extracted along Horizon H5, showing the scours and boundaries of MTC-3. RGB Blending is applied as 45Hz, 50Hz, and 60Hz. (d) Interpreted sketch of MTC-3, showing its boundaries, key kinematic indicators, and transport direction.

Figure 6. (a) Variance horizon slice through the area with semi-rounded, crater-like depressions (25ms above Horizon H5). See Figure 5d for the extent of Figure 6a. (b) Spectral decomposition slice through the area with semi-rounded, crater-like depressions (25ms above Horizon H5). See Figure 5d for the extent of Figure 6b. (c) Uninterpreted section B-B' showing the seismic characteristics of semi-rounded, crater-like depressions. (d) Interpreted sketch of section B-B', showing the high-angle deformation characteristics indicative of fluid escape pipes.

Figure 7. Multi-well correlation showing the log responses of MTCs, free gas-bearing sediments, and hydrate-bearing sediments. GR: gamma ray; TNPH: thermal neutron porosity; DEN: bulk density; RES_BS: shallow button resistivity; RES_BD: deep button resistivity; *Vp*: P-wave velocity; Gas Vol: undisturbed zone gas volume fraction; DHAT: downhole annulus temperature. See **Appendix C** for details of hydrate saturation calculations.

Figure 8. Petrophysical differences between MTC-1 over flat topography and MTC-1 over topographic highs. (a) density; (b) resistivity; (c) porosity; (d) permeability. The data are retrieved from well log data in the interval between horizon H1 and H2, see Figure 2 and Figure 7 for more details. The depth of color reflects the kernel density which is a measurement of data tendency.

Figure 9. Numerical simulation showing shear strain distribution in MTCs under different topographies: (a) flat topography; (b) frontal ramp; (c) remnant block.

Figure 10. The role of shear localization in controlling seal integrity of MTCs. (a) Three-dimensional sketch showing the effect of topographic highs on shear localization development; (b) microscopic

change of pore structure when shear is weakened; (c) microscopic change of pore structure when shear is strengthened.

Figure 11. Three-dimensional schematic diagram showing the methane-bearing fluid migration pathways. Reddish yellow arrows indicate the migration of methane-bearing fluid. The upper surface of the seismic volume is a composite of two time slices at 2,490 ms and 2,536 ms in TWT to manifest three BSRs. Horizon slices of H1, H3, and H5 are presented to show the basal shear surfaces of MTCs. BD: background deposit.

Figure A1. Demonstration of seismic-well tie using well W1 as an example.

Parameters	Notation	Unit	Value
Length of slope	L	m	4,800
Slope angle	α	$degree$	1.2
Density	ρ	$Kg \cdot m^{-3}$	1,700
Gravity acceleration	g	$m \cdot s^{-2}$	9.81
Yield stress	τ_0	Pa	8,000
Reference strain rate	$\dot{\varepsilon}_r$	s^{-1}	0.1
Flow index	n	/	0.75
Numerical grid resolution	n_x	/	511
	n_y	/	127
CFL coefficient	CFL	/	0.2

Table 1

Amplitude anomaly	Petrophysical properties				Interpretation
	Density	Resistivity	P-velocity	Temperature	
BSR 1	Low ~1.6 g/cm^3	Slightly high ~2 Ωm	Low ~1,600 m/s	High ~8 ^oC	Free gas sourced from the Songnan Low Uplift
BSR 2	Slightly high ~1.85 g/cm^3	High ~200 Ωm	High ~2,300 m/s	Low ~2 ^oC	High-saturation gas hydrate (~90% saturation)
BSR 3	Moderate ~1.8 g/cm^3	Slightly high ~2 Ωm	Slightly low ~1,700 m/s	High ~9 ^oC	Coexistence of free gas and low-saturation gas hydrate (~10% saturation)

Table 2

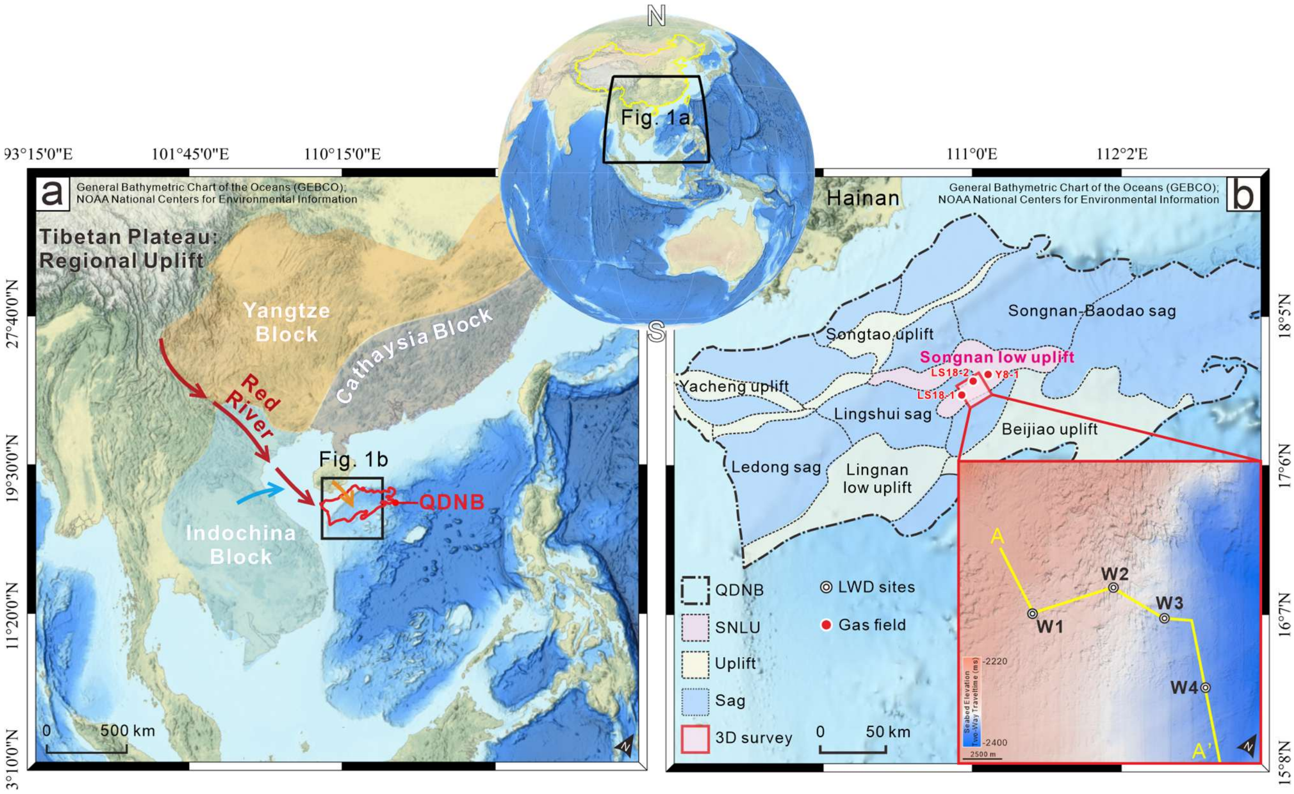
N
S
Fig. 1a
93°15'0"E
101°45'0"E
110°15'0"E
111°0'E
112°2'E
27°40'0"N
19°30'0"N
11°20'0"N
3°10'0"N
18°5'N
17°6'N
16°7'N
15°8'N
a
General Bathymetric Chart of the Oceans (GEBCO);
NOAA National Centers for Environmental Information
Tibetan Plateau:
Regional Uplift
Yangtze
Block
Cathaysia Block
Red
River
Indochina
Block
Fig. 1b
QDNB
0
500 km
b
Hainan
Songnan-Baodao sag
Songtao uplift
Songnan low uplift
LS18-2
Y8-1
LS18-1
Yacheng uplift
Lingshui sag
Beijiao uplift
Ledong sag
Lingnan
low uplift
QDNB
SNLU
Uplift
Sag
3D survey
LWD sites
Gas field
0
50 km
A
W1
W2
W3
W4
A'
-2220
-2400
2500 m

Figure 1

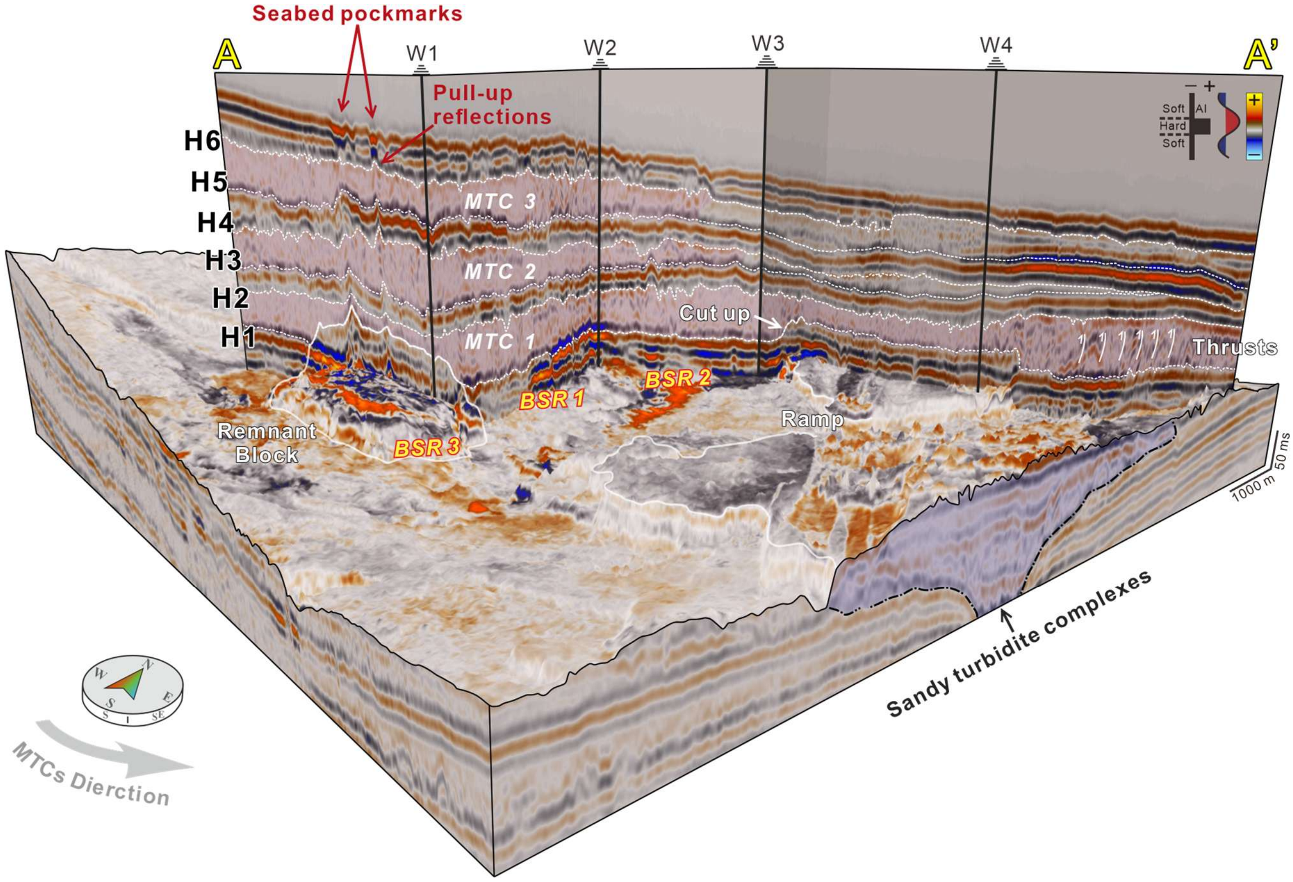

Seabed pockmarks
Pull-up
reflections
A
W1
W2
W3
W4
A’
Soft
Hard
Soft
AI
H6
H5
H4
H3
H2
H1
MTC 3
MTC 2
MTC 1
Cut up
Thrusts
BSR 1
BSR 2
BSR 3
Remnant
Block
Ramp
50 ms
1000 m
Sandy turbidite complexes
MTCs Dierction

Figure 2

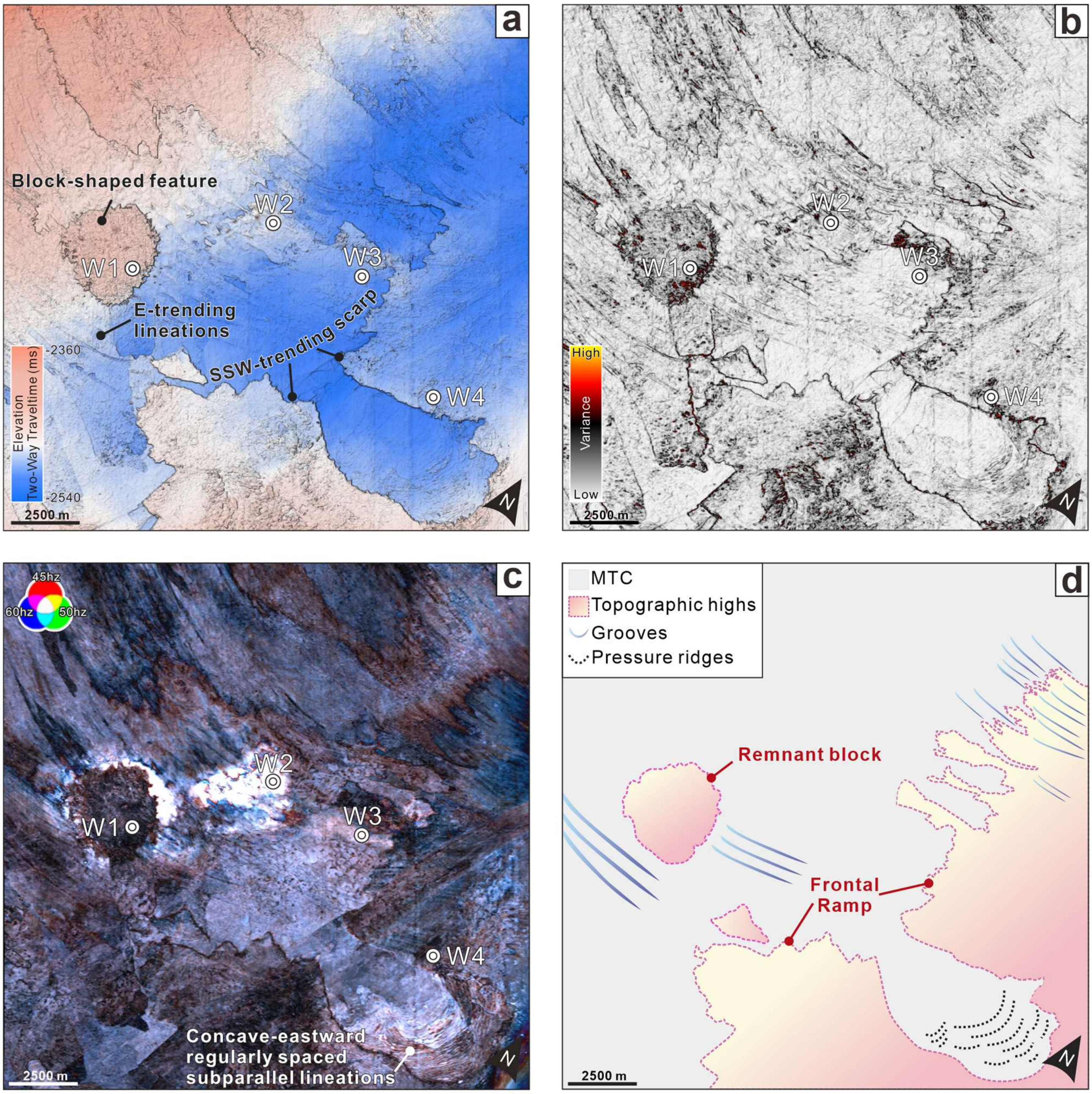
a
Block-shaped feature
W1
W2
W3
W4
E-trending
lineations
SSW-trending scarp
-2360
-2540
Elevation
Two-Way Traveltime (ms)
2500 m
N
b
W1
W2
W3
W4
High
Variance
Low
2500 m
N
c
45hz
60hz
50hz
W1
W2
W3
W4
Concave-eastward
regularly spaced
subparallel lineations
2500 m
N
d
MTC
Topographic highs
Grooves
Pressure ridges
Remnant block
Frontal
Ramp
2500 m
N

Figure 3

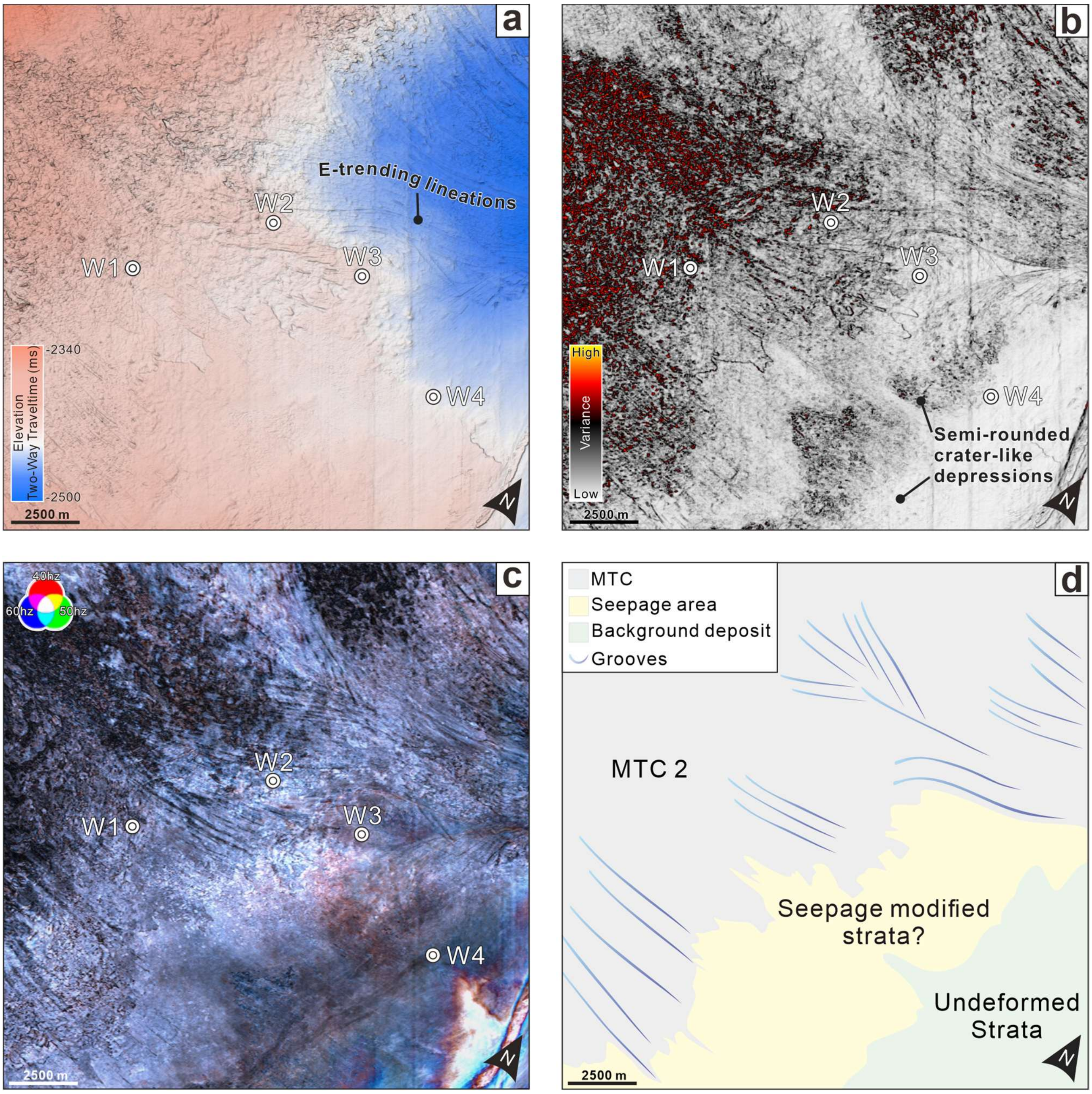
a
E-trending lineations
W1
W2
W3
W4
-2340
-2500
Elevation
Two-Way Traveltime (ms)
2500 m
N
b
W1
W2
W3
W4
High
Variance
Low
Semi-rounded
crater-like
depressions
2500 m
N
c
40hz
60hz
50hz
W1
W2
W3
W4
2500 m
N
d
MTC
Seepage area
Background deposit
Grooves
MTC 2
Seepage modified
strata?
Undeformed
Strata
2500 m
N

Figure 4

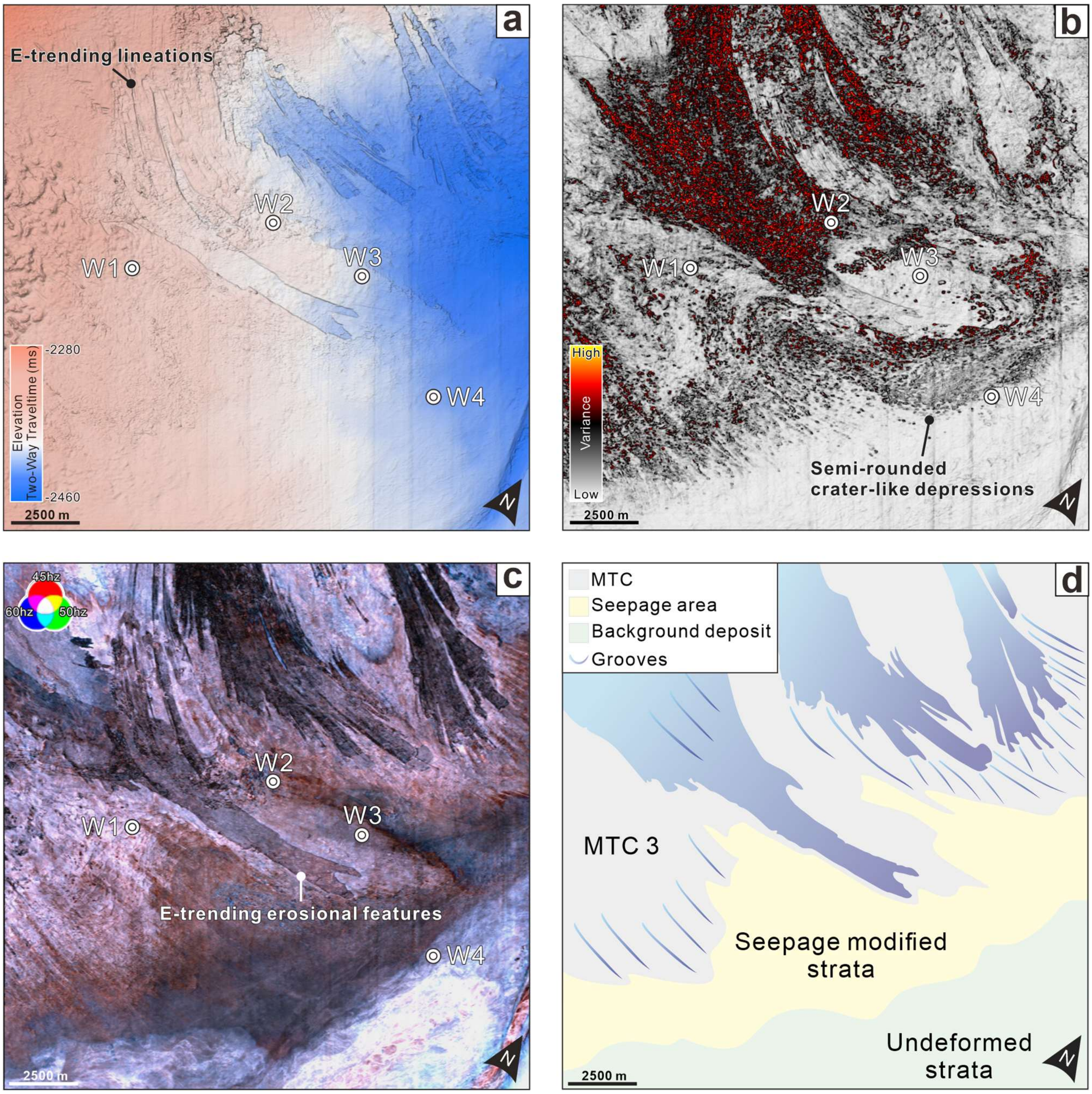
a
E-trending lineations
W1
W2
W3
W4
Elevation
Two-Way Traveltime (ms)
-2280
-2460
2500 m
N
b
W1
W2
W3
W4
High
Variance
Low
Semi-rounded
crater-like depressions
2500 m
N
c
45hz
60hz
50hz
W1
W2
W3
W4
E-trending erosional features
2500 m
N
d
MTC
Seepage area
Background deposit
Grooves
MTC 3
Seepage modified
strata
Undeformed
strata
2500 m
N

Figure 5

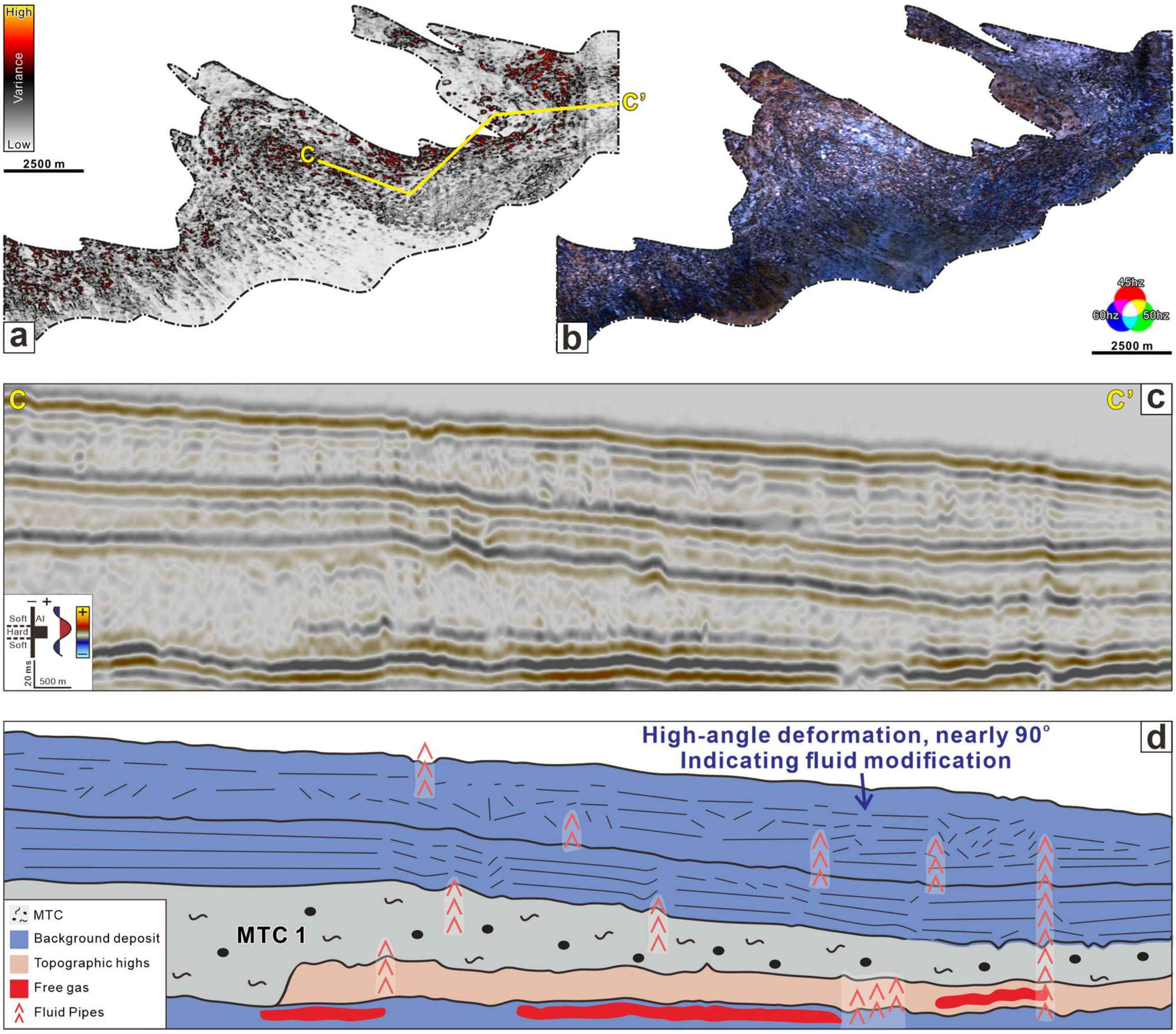
High
Variance
Low
2500 m
C
C'
a
b
45hz
60hz
50hz
2500 m
C
C'
c
Soft
Hard
Soft
AI
20 ms
500 m
d
High-angle deformation, nearly 90°
Indicating fluid modification
MTC 1
MTC
Background deposit
Topographic highs
Free gas
Fluid Pipes

Figure 6

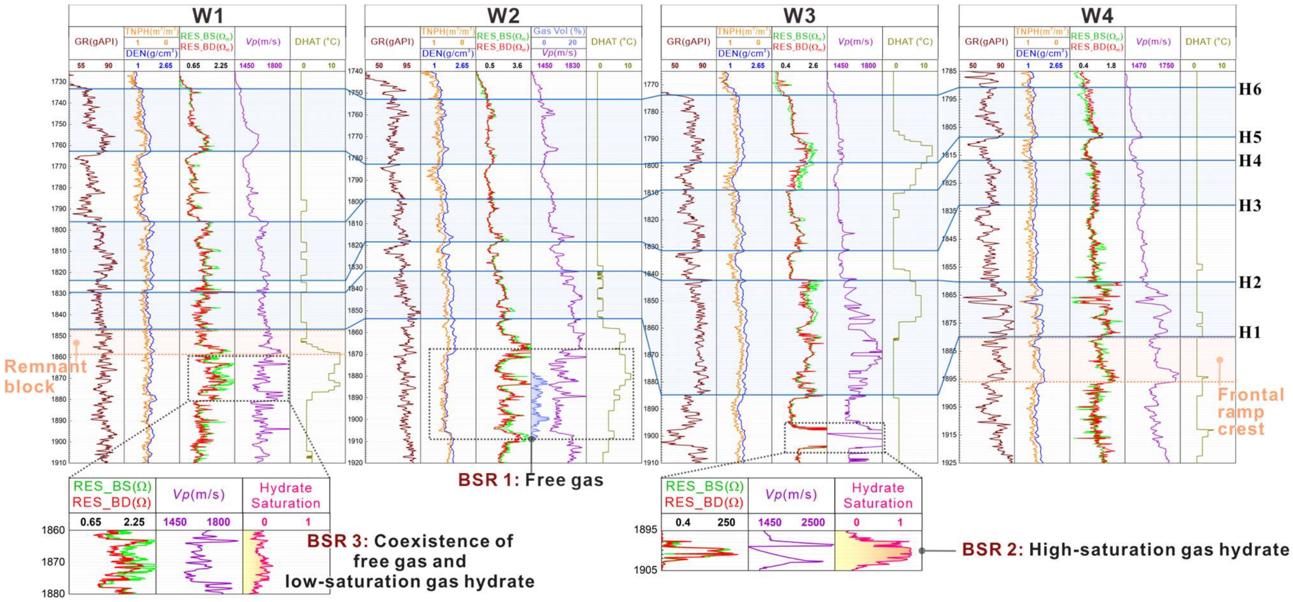
W1
W2
W3
W4
GR(gAPI)
TNPH(m³/m³)
DEN(g/cm³)
RES_BS(Ωm)
RES_BD(Ωm)
Gas Vol (%)
Vp(m/s)
DHAT (°C)
H6
H5
H4
H3
H2
H1
Remnant block
Frontal ramp crest
Hydrate Saturation
BSR 1: Free gas
BSR 2: High-saturation gas hydrate
BSR 3: Coexistence of free gas and low-saturation gas hydrate

Figure 7

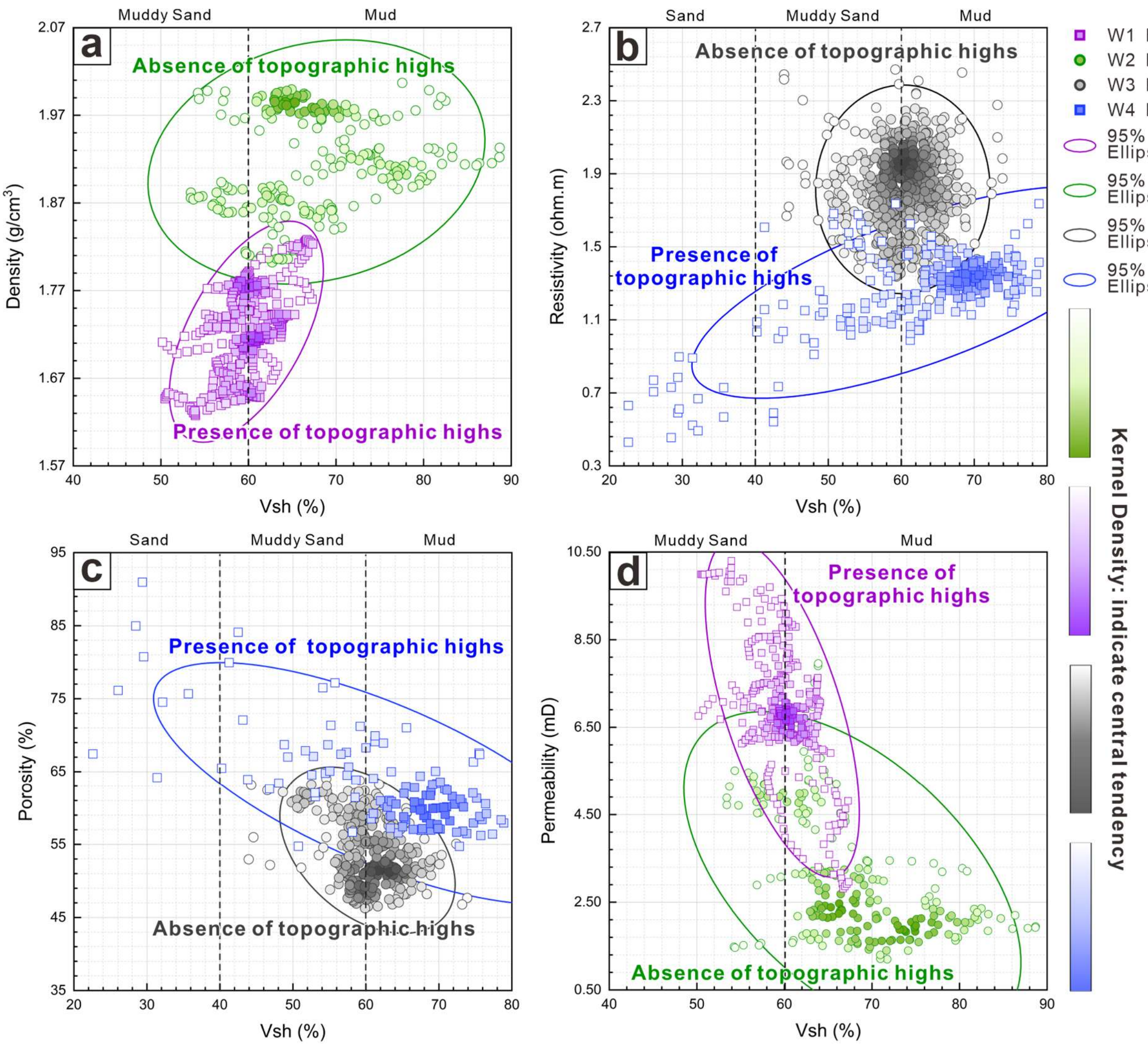
a
Muddy Sand
Mud
Absence of topographic highs
Presence of topographic highs
Density (g/cm3)
Vsh (%)
b
Sand
Muddy Sand
Mud
Absence of topographic highs
Presence of topographic highs
Resistivity (ohm.m)
Vsh (%)
c
Sand
Muddy Sand
Mud
Presence of topographic highs
Absence of topographic highs
Porosity (%)
Vsh (%)
d
Muddy Sand
Mud
Presence of topographic highs
Absence of topographic highs
Permeability (mD)
Vsh (%)
W1 H1-H2
W2 H1-H2
W3 H1-H2
W4 H1-H2
95% Confidence Ellipse for W1
95% Confidence Ellipse for W2
95% Confidence Ellipse for W3
95% Confidence Ellipse for W4
Kernel Density: indicate central tendency

Figure 8

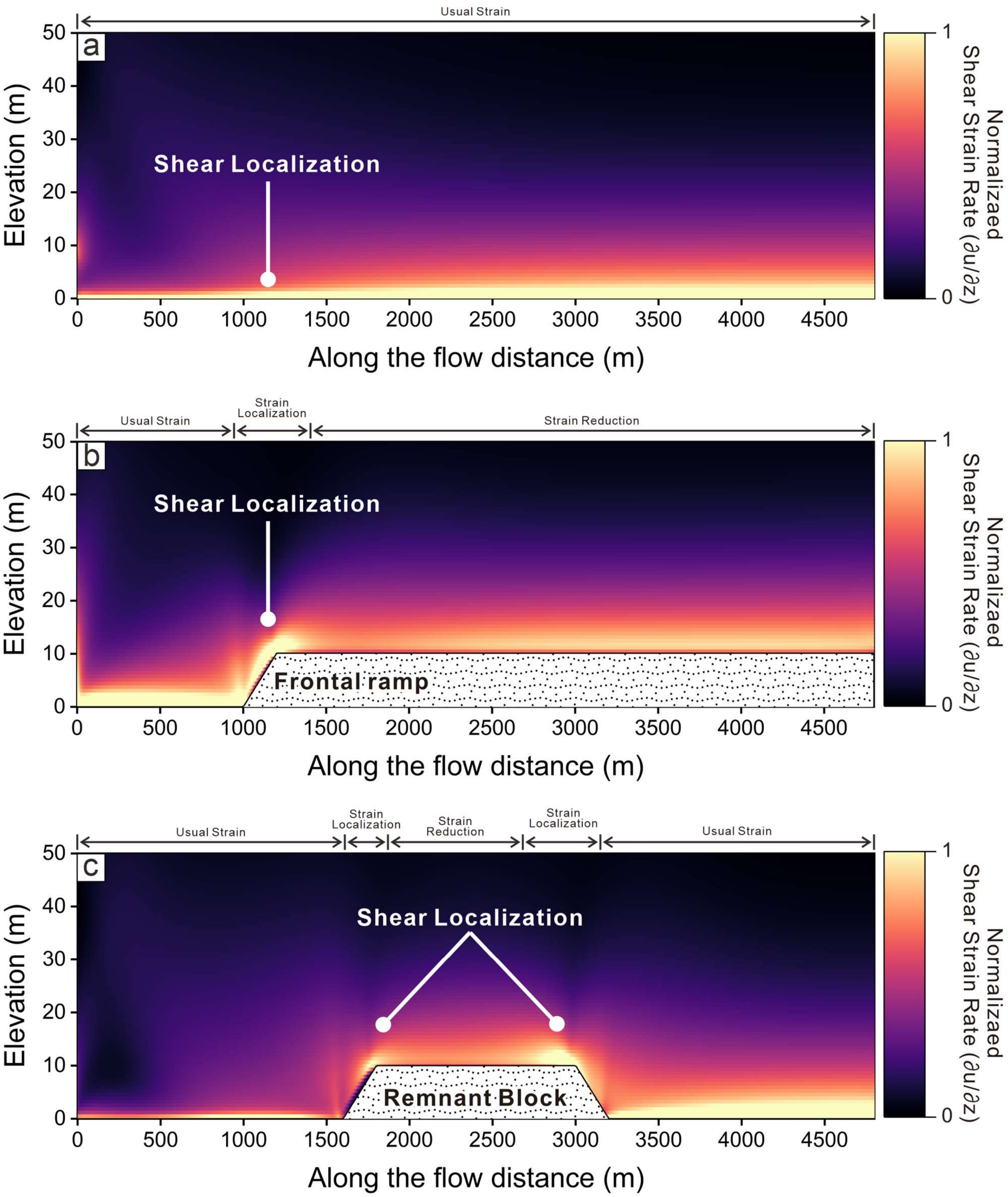
Usual Strain
a
Shear Localization
Elevation (m)
Along the flow distance (m)
Normalizaed Shear Strain Rate (∂u/∂z)
Usual Strain
Strain Localization
Strain Reduction
b
Shear Localization
Frontal ramp
Elevation (m)
Along the flow distance (m)
Normalizaed Shear Strain Rate (∂u/∂z)
Usual Strain
Strain Localization
Strain Reduction
Strain Localization
Usual Strain
c
Shear Localization
Remnant Block
Elevation (m)
Along the flow distance (m)
Normalizaed Shear Strain Rate (∂u/∂z)

Figure 9

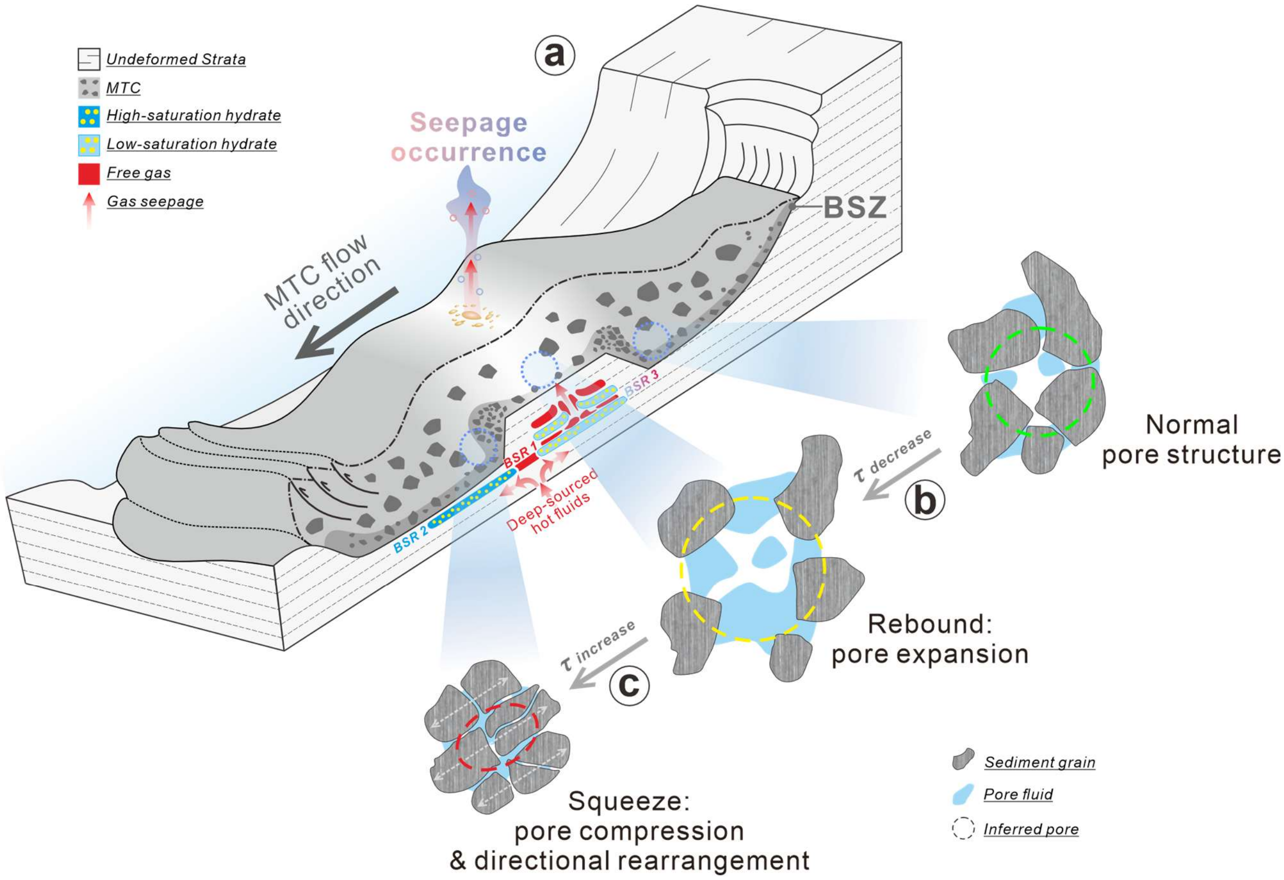

807

808 Figure 10

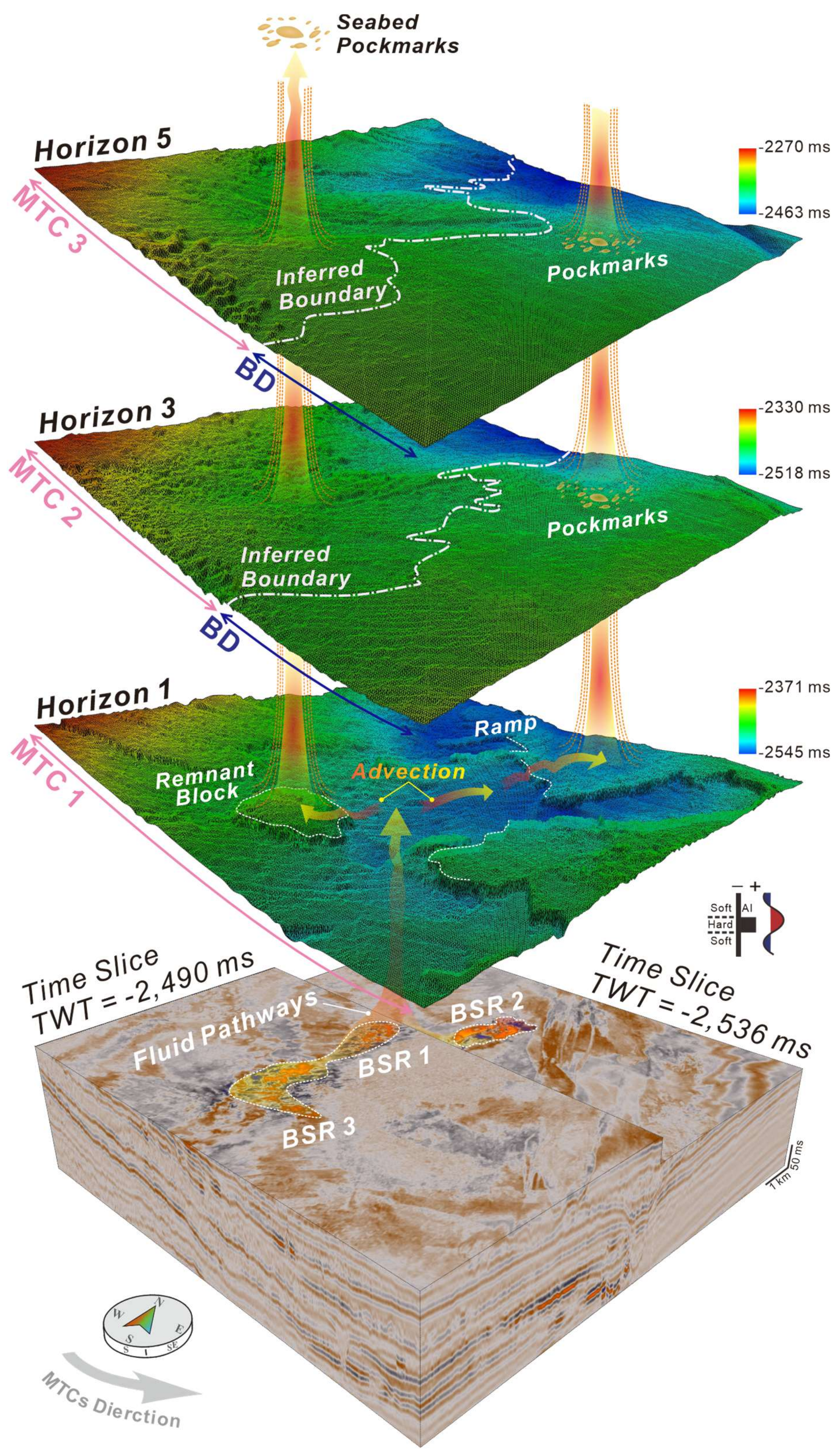

Seabed Pockmarks
Horizon 5
MTC 3
Inferred Boundary
Pockmarks
-2270 ms
-2463 ms
BD
Horizon 3
MTC 2
Inferred Boundary
Pockmarks
-2330 ms
-2518 ms
BD
Horizon 1
MTC 1
Remnant Block
Advection
Ramp
-2371 ms
-2545 ms
Soft
Hard
Soft
AI
Time Slice
TWT = -2,490 ms
Time Slice
TWT = -2,536 ms
Fluid Pathways
BSR 1
BSR 2
BSR 3
1 km
50 ms
MTCs Dierction

Figure 11

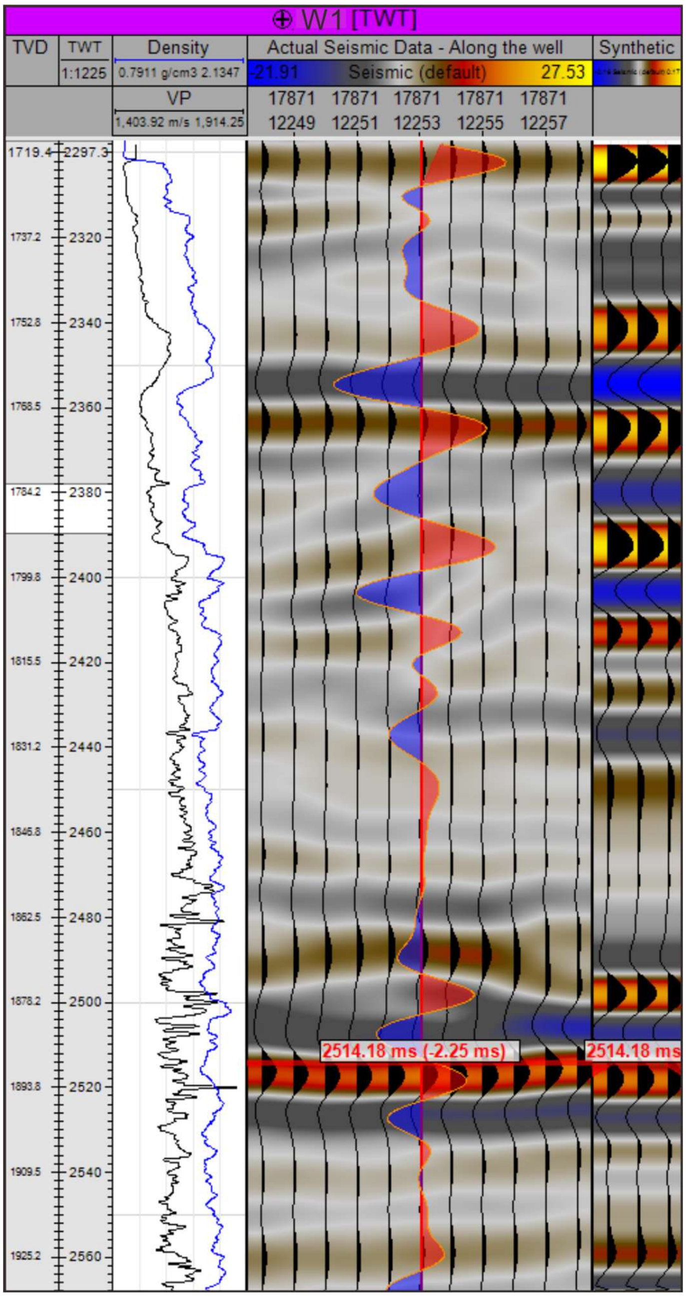

W1 [TWT]
TVD
TWT
1:1225
Density
0.7911 g/cm3 2.1347
VP
1,403.92 m/s 1,914.25
Actual Seismic Data - Along the well
-21.91
Seismic (default)
27.53
17871 12249
17871 12251
17871 12253
17871 12255
17871 12257
Synthetic
1719.4 2297.3
1737.2 2320
1752.8 2340
1768.5 2360
1784.2 2380
1799.8 2400
1815.5 2420
1831.2 2440
1846.8 2460
1862.5 2480
1878.2 2500
1893.8 2520
1909.5 2540
1925.2 2560
2514.18 ms (-2.25 ms)
2514.18 ms

Figure A1